https://doi.org/10.15407/ufm.25.04.822

D.A. LESYK [1,2,3,*], B.M. MORDYUK [2,4,], W. ALNUSIRAT [5,***], S. MARTINEZ [1,****], V.V. DZHEMELINSKYI [1], O.O. GONCHARUK [1], P.V. KONDRASHEV [1], Yu.V. KLYUCHNIKOV [1], and A. LAMIKIZ [3]**

[1] National Technical University of Ukraine
'Igor Sikorsky Kyiv Polytechnic Institute',
37 Prospect Beresteiskyi, UA-03056 Kyiv, Ukraine
[2] G.V. Kurdyumov Institute for Metal Physics of the N.A.S. of Ukraine,
36 Academician Vernadsky Blvd., UA-03142 Kyiv, Ukraine
[3] University of the Basque Country,
1 Plaza Ingeniero Torres Quevedo, SP-48013 Bilbao, Spain
[4] E.O. Paton Electric Welding Institute of the N.A.S. of Ukraine,
11 Kazymyr Malevych Str., UA-03150 Kyiv, Ukraine
[5] Al-Balqa Applied University,
33 Salt St., JO-19117 Al-Salt, Jordan

* lesyk_d@ukr.net, dmytro.lesyk@ehu.eus, ** mordyuk@imp.kiev.ua,
*** walidnusir@bau.edu.jo, **** silvia.martinez@ehu.eus

ULTRASONIC SURFACE FINISHING OF AISI 1045 STEEL HARDENED BY LASER HEAT TREATMENT WITH FIBRE LASER AND SCANNING OPTICS: LAYERED-STRUCTURE-INDUCED HARDENING AND ENHANCED SURFACE MORPHOLOGY

Nowadays, emerging of new technologies causes implicitly the increased requirements for conventional methods and materials. Literature survey shows that combined thermomechanical processes of surface hardening and finishing using highly-concentrated energy sources are promising to enhance the surface integrity and operational properties of structural steels. Some surface-related and microstructural factors can be

Citation: D.A. Lesyk, B.M. Mordyuk, W. Alnusirat, S. Martinez, V.V. Dzhemelinskyi, O.O. Honcharuk, P.V. Kondrashev, Yu.V. Kliuchnykov, and A. Lamikiz, Ultrasonic Surface Finishing of AISI 1045 Steel Hardened by Laser Heat Treatment with Fibre Laser and Scanning Optics: Layered-Structure-Induced Hardening and Enhanced Surface Morphology, *Progress in Physics of Metals*, **25**, No. 4: 822–867 (2024)

considered crucial for properties' enhancement, *viz.*, surface roughness and waviness, grain size and phase composition, residual macrostresses, and microhardness. In this work, a laser heat treatment (LHT) followed by an ultrasonic impact treatment (UIT) also known as high-frequency mechanical impact (HFMI) treatment is sequentially applied to the AISI 1045 steel to demonstrate the efficiency of their combined influence. The near-surface microstructure formed after the combined LHT + UIT process is observed by optical microscopy, transmission electron microscopy, and x-ray diffraction analysis. The surface residual macrostresses, microhardness, roughness, and waviness are also evaluated. The results show that the combined LHT + UIT-treatment induces phase transformation and severe plastic deformation, forming layered hardening and grain structure refinement in the near-surface layers of medium-carbon steel. The subsurface microhardness at a depth up to ≈50 μm after the combined treatment is significantly increased (>10 GPa) due to the severe plastic deformation of the LHT-formed martensitic lamellas, providing the nanoequiaxed grain microstructure in the subsurface layer. The hardening depth (140–440 μm) in the LHT + UIT-treated samples depends on the LHT speed (40–140 mm/min) and the heating temperature (1200–1300 °C) by scanning laser beam. Additionally, taking into account the surface residual compressive macrostresses (>400 MPa), smoother microrelief on the surface, and reduced roughness parameters (Ra < 0.5 μm) formed by UIT, the studied steel functionality is expected to be improved. The combined laser–ultrasonic surface hardening and finishing process can be used for large-size steel product treatment.

Keywords: AISI 1045, combined surface treatment, laser phase-transformation hardening, ultrasonic finishing, gradient structure, surface nanostructuring, surface morphology.

1. Introduction

Advanced metal/composite materials and technologies are currently developed to meet the growing needs of modern industry and reduce the use of natural resources, providing higher operational properties of responsible metallic products. It is well known that the use of expensive wear-resistant and corrosion-resistant materials to solve the problem of increasing the reliability and durability of critical metal parts is economically impractical [1–3]. Structural steels remain key materials for a variety of applications in mechanical engineering and toolmaking [4]. The fabrication process methods and the chemical composition of steels can affect their mechanical properties and corrosion/wear resistance [5–7] and the strength of the produced components accordingly [8, 9]. At the same time, the use of traditional manufacturing methods does not always allow for obtaining the required surface integrity and quality for structural steel parts that work in extreme conditions [10]. The extension of the operation life of the structural materials by preventing their degradation during cyclic loading under extreme conditions or corrosive environments remains very relevant. The quality of the surface layer of mid-to-high-carbon steels is simultaneously determined by geometrical parameters (surface texture, roughness, and waviness), and physical-mechanical proper-

ties (phase composition, structure, grain size, microhardness, and residual macrostresses), is one of the important characteristics that affect both the corrosion/wear resistance and fatigue life of the manufactured steel products. As a result, the development and continual improvement of advanced surface technologies for enhancing iron–carbon alloys is a vital resource in the production processes, providing the required near-surface structure and properties.

The formation of favourable phase/stress states and near-surface nanostructures through the parameter optimization of surface post-treatment methods is an effective strategy to enhance further the wear and corrosion resistance of structural steels. One of the most promising directions is the improvement of modern manufacturing processes using advanced surface treatment methods, such as electron beam hardening [11, 12], plasma hardening [13–16], and laser hardening [17–21], or combination of them with other relevant surface treatment methods [22–28]. Such a comprehensive approach will significantly improve both the physical and mechanical properties and surface roughness of steel products.

Compared to the traditional solid phase transformation processes, such as induction [29] and flame heat treatment [30]), the high-quality and localized surface hardening methods using highly-concentrated energy sources (plasma jet [13, 16, 31–34], electron beam [11, 35–38], and laser beam [17, 19, 39–46]) are effective and precise tools to improve significantly the performance of steel components due to controlled changes in the structure and phase state of the near-surface layer. The abovementioned surface phase transformation hardening methods are based on the heating to a certain temperature (below the melting temperature of treated iron–carbon alloy) of selected surface areas and subsequent rapid cooling at a very high rate, forming a fine crystalline microstructure in the near-surface layer [47–50]. When a thin metal layer of steel is heated rapidly and locally to a temperature above the austenitization A_{C3} (A_{Cm}) temperature points, phase, and structural transformations occur. In particular, the formation of austenite (the transformation of the $\alpha + \mathrm{FeC}$ phase into the $\gamma + \mathrm{Fe}$ phase) occurs during the heating cycle, while the transformation of austenite into martensite during the cooling cycle is due to the heat transfer in the inner layers of the material.

The hardened areas of structural steels without melting (the solid phase processes ($T < T_{\mathrm{M}}$)) by plasma jet and electron/laser beam usually consist of several gradient layers: hardening zone, transition zone, heat affected zone (HAZ), and base material [32, 51, 52]. The thickness of the hardened surface layer depends on the speed at which the plasma jet or electron/laser beam is moved over the workpiece surface. The thicker hardened surface layer is formed at a slower speed. The method of increasing the durability of structural steel products due to selective surface hardening of their working areas using highly concentrated energy sourc-

es is becoming extremely relevant and important in mechanical engineering. As a result of this process, a hard wear-resistant surface is formed on selected areas of the processed part due to the formation of a martensite microstructure in the iron–carbon alloys as a product of solid-state phase transformation [11, 16, 35, 53–56].

The surface hardness of the heat-treated steel parts depends on the temperature–time-dependent phase changes and the changes in carbon solubility caused by solid-state phase transformations [44, 57–59]. Compared to the electron-beam/plasma/laser hardening techniques, based on rapid heating and cooling cycles, the diffusion of carbon into steel takes several stages during the conventional heat treatment to form the metastable martensite [60]. The surface morphology and dimension tolerances are not changed after surface hardening without melting the workpiece surface by plasma jet and electron/laser beam [61]. However, the roughness parameters may change slightly due to an oxide layer formation, if the surface treatment is not carried out in a protective environment [46, 62].

The electron-beam heat treatment (EBHT) is one of the effective techniques for surface modification of steel parts of complex shapes or small-size metallic components [11]. This environmentally friendly surface hardening technology ensures a constant depth of hardening along two axes, the lack of the formation of oxide films on the surface, a high-efficiency coefficient, and EBHT process productivity. The EBHT treatment is based on the use of the energy of a focused flow of electrons (0.1–0.4 mm-focused electron beam in diameter) generated by an electron gun [35, 36] under high vacuum conditions. During EBHT treatment without melting of steel surfaces with a power density of 10^2–10^4 W/cm^2 at a heating duration of 1–10 s in a vacuum, the thickness of the hardened layer can be achieved up to 2.5 mm [35]. Wei *et al.* [38] obtained the hardened surface layer of 5CrMoMn steel with a hardness of ≈650 *HV* by the continuous scanning electron beam process. Similarly, the authors of Refs. [11, 36, 37] studied the effects of the EBHT process parameters on the hardening zone, microstructure, and hardness of 30CrMnSiA, 40X, and 40CrMn steels. In general, a finer martensitic structure with different percentages of retained austenite is formed due to high heating and cooling rates, increasing the surface hardness of the studied steels. The formed martensitic microstructure in the EBHT-hardened hypereutectoid steels contains a lath-like morphology with small packets of nearly parallel short laths [12].

The plasma heat treatment (PHT) is another advanced surface hardening method that is mainly used for the surface treatment of large-size carbon steel components. Unlike EBHT treatment, the PHT treatment is more widely used in industry for surface hardening of steel parts due to its much lower cost and ease of use. The plasma hardening of steels by the action of low-temperature plasma consists of local heating of the surface layer by a plasma arc with a power density of 10^3–10^5 W/cm^2 and subse-

quent cooling by removal of the plasma energy *via* conduction [32]. The PHT process is based on the use of the energy of the plasma jet, which is formed when special plasma-forming gases are passed through an electric arc discharge. The effective efficiency of heating is 40–80% [13]. The PHT treatment of steel without melting the surface makes it possible to harden the surface layer to a depth of 0.5–2.5 mm, depending on the process parameters and the type of the treated material, increasing the surface microhardness ≈850 *HV*, which increases the wear resistance of hardened surfaces by 2–4 times [31, 33, 34, 63]. In addition, similar to laser surface hardening systems, the developed quasi-laminar or laminar plasma jet hardening systems provide controllability and repeatability to produce the hardened layer with the desired microstructure and hardness gradient [13, 32]. The PHT treatment is successfully used for the surface hardening of rail wheels, rolling shafts, die tools, bushings, drilling tools, and others [32].

Transformation hardening is among other surface treatments made possible by laser as well. The high heating and cooling rates (10^8–10^{10} °C/s) are activated during a laser heat treatment (LHT) with a power density of 10^3–10^4 W/cm^2 to harden selectively the surfaces, enhancing the mechanical properties of the structural steels due to the fine-grained microstructure formation in the near-surface layers [41, 47, 51, 56]. It should also be noted that the martensitic-austenitic structure formation depends on the laser surface hardening regimes and the carbon concentration in the alloy. Increasing the concentration of carbon in the carbon steels is accompanied by an increase in the hardening depth through calcination increment. Conversely, reducing the hardening depth and increasing the hardening width in the carbon steels occurs with increasing the carbon content due to the reduction of thermal conductivity [62].

New laser surface hardening systems using modern lasers with high-quality laser beams, scanning optics, and optimized shielding gas protection of the laser beam in the processing area are now showing lower operational costs and better efficiency than those laser systems using older CO_2 and Nd:YAG lasers [48, 64]. The effect of laser surface hardening with conventional lasers on the layered structure and phase transformation features [65–67], HAZ and hardness distribution [68], as well as residual stress state [69] of structural steels were widely studied. Compared to the conventional laser surface hardening systems, advanced high flexibility laser hardening systems using a diode laser [47, 57, 70, 71] and fibre laser [22, 43, 72–74] or disk laser [18, 20, 75, 76] coupled with scanning optics significantly increases the productivity and efficiency of the LHT treatment for both small-sized and large-scale carbon steel parts. The diode and fibre lasers bring the available power to a level usable by a wide range of material processing. At the same time, the application of high-tech 2*D*-scanning optics [52, 61] and 3*D*-scanning optics [72–74, 76] com-

bined with high-power lasers increases the laser spot size of more than 50 mm. In most cases, it allows for avoiding the overlapping of the laser beam, which causes the heterogeneous hardness in the subsurface layers of steel parts via the tempered martensitic microstructure formation in the overlapping area of the laser beam [43, 77, 78]. It should also be noted that the robot-assisted 3*D*-scanning laser hardening systems demonstrate easier automation as compared to the EBHT and PHT methods [18, 20, 72, 74–76]. The use of advanced high-power lasers to harden the surface of steel end-products to increase the resistance to wear [62, 79–83], corrosion [51, 52, 84, 85], fatigue [40, 86], heat, and erosion has significant growth potential for manufacturing industries using advanced laser surface hardening systems.

It should also be noted that the single electron-beam surface hardening, plasma surface hardening, and laser surface hardening using conventional lasers have mainly reached their threshold of development for surface treatment of the structural steels. Therefore, a large number of manufacturers and researchers have directed their efforts to develop combined and hybrid techniques for surface hardening to improve the material properties. For example, the EBHT method was combined with the thermochemical treatment (carburizing, nitriding, nitrocarburizing, boriding), forming hard protective coatings [11, 12, 87–90]. To increase significantly the fatigue life and wear resistance of structural steels, the combined/hybrid thermomechanical surface hardening and finishing techniques are developed using the PHT and LHT processes combined with surface plastic deformation (SPD) methods, such as friction stir processing [91], ball-burnishing [92–94], shot peening [95–97], laser shock peening [98, 99], ultrasonic nanocrystal surface modification [98, 100–104], and ultrasonic impact peening [22, 50, 52, 105, 106]. The combined/hybrid surface thermomechanical hardening and finishing technologies have significant potential to be more often used in the fabrication processes for the surface treatment of structural steel components. An emerging tendency of current approaches consists of combining various techniques (thermal, mechanical, and chemical-related ones) to achieve maximum beneficial influence on the targeted property of the modified steels, and these techniques can be applied either simultaneously or in a sequential manner. The advanced combined methods applied to the product surface using the surface treatment by highly-concentrated energy sources combined with severe plastic deformation may significantly improve the surface roughness and physical-mechanical properties of the modified surface layer.

Based on the literature review, the use of laser surface hardening combined with ultrasonic impact peening or ultrasonic nanocrystal surface modification methods allows a significantly greater effect in increasing the strength, reliability, and durability of the surface layer due to the formation of the near-surface ultrafine-grained microstructure [52, 80],

compressive residual macrostresses on the surface [106] and surface microrelief with a reduced surface roughness [46, 61]. In this regard, the present work is focused on studying the effects of the high-temperature laser surface hardening (1200–1300 °C) with a 1 kW fibre laser and scanning optics combined with severe ultrasonic impact treatment by a multi-pin ultrasonic tool with different peening intensity on the surface properties of AISI 1045 steel, which is used in numerous industrial applications. The main objective is to analyse the microstructural features, phase and residual stress state, sub-surface gain size, surface microhardness, sizes of hardening areas, surface texture, surface roughness, and waviness parameters after the combined laser-ultrasonic treatment.

2. Experimental Methods

The medium-carbon steel was selected as the feedstock material in this study. Carbon steels are widely used as structural materials in mechanical engineering for the production of responsible components requiring enhanced surface integrity, strength, and wear/corrosion resistance [107]. Prior to surface treatments, the plane test specimens with dimensions of $100 \times 60 \times 20$ mm^3 were heated to 850 °C; then, they were slowly cooled in the furnace to 650 °C (10 °C per hour).

In the initial state, the microstructure of the AISI 1045 steel consisted of ferrite and perlite. Then, the studied specimens were polished ($Ra \approx 0.6$ μm) before surface treatments to remove the carbonaceous layer and prepare the surface for close production conditions. The chemical composition of the studied steel is listed in Table 1 [79, 108]. The average surface macrohardness and microhardness values of the studied steel are ≈18.5 HRC_5 and ≈300 $HV_{0.05}$, respectively.

Table 1. **Chemical composition data of the AISI 1045 steel**

Chemical element	C	Mn	Si	Cr	Ni	Cu	Fe
Weight percentage	0.45	0.75	0.27	≤0.25	≤0.25	≤0.25	balanced

Table 2. **Laser surface treatment parameters**

Regime abbreviation	Heating temperature, °C	Measured average power, W	Specimen feed rate, mm/min	Scanning speed, mm/s
LHT1	1200	680	40	1000
LHT2	1200	690	90	
LHT3	1200	730	140	
LHT4	1300	700	40	
LHT5	1300	730	90	
LHT6	1300	780	140	

2.1. Methodological Details

The LHT of the test specimens was implemented by single passes using a 1 kW fibre laser (Rofin Sinar FL010) with a wavelength of 1.07 μm, a high-frequency scanning optics (Scanlab Hurry Scan 25), and a milling centre (Kondia Aktinos B500) with computer numerical control (CNC) specially designed for the scanner-based laser surface hardening process [22, 44, 46, 52, 56]. A schematic illustration of the scanner-based laser hardening process with the heating temperature control used is shown in Fig. 1. The LHT parameters are listed in Table 2.

The 2*D* laser surface hardening system developed based on the CNC centre allowed for moving the processed test specimens along the *XY* axes with a total working area of 500×300 mm. The laser radiation was transported to the optical system using a 100 μm-diameter optical fibre, which provided a 100 μm-diameter laser spot and multimode energy distribution in the focal plane. The used optical 2*D* system with a flat lens allowed the scanning of the laser beam in a focal plane of 120×120 mm. LHT of the samples was carried out in the continuous wave mode with defocusing of the laser beam in the working plane to 1 mm. The defocusing distance of the working plane was equal to 50 mm. A schematic view of the scanning of the laser beam is demonstrated in Fig. 1. All LHT tests were performed in an ambient atmosphere without any shielding gases.

To avoid the melting of the surface layer of the studied steel, a proportional-integral-derivative (PID) controller was integrated using special software and an optical pyrometer (Impac Igar 12LO) to measure and control the surface temperature in the hottest zone of the laser track (Fig. 1). The PID controller adjusted the power signal each 50 ms to keep the nominal temperature during the LHT treatment. The measured average power values are given in Table 2. The two-coloured pyrometer was moved simultaneously with the optical system. Thus, the LHT applying the constant temperature strategy is carried out, which, in contrast to the constant power strategy, allows for avoiding undesirable surface melting (the melting temperature of 1045 steel is ≈1450 °C) in the sites where the processed components dimensions are markedly changed. Additionally, the LHT process was monitored using a high-speed video camera. The PID temperature control system used was described in more detail elsewhere [22, 44, 61].

In this study, the LHT process without applying absorbent coatings was carried out at a sample heating temperature of 1200–1300 °C, laser beam spot of 1 mm, and specimen feed rate of 40–140 mm/min, providing duration of the laser action of 1.5–0.42 s on the LHT-treated area (Fig. 2). LHT duration was calculated by the ratio of the laser spot (d, mm) to the sample feed rate (S, mm/s). The scanning speed and scanning width of the laser beam were constant. The LHT parameters applied are listed in Table 2.

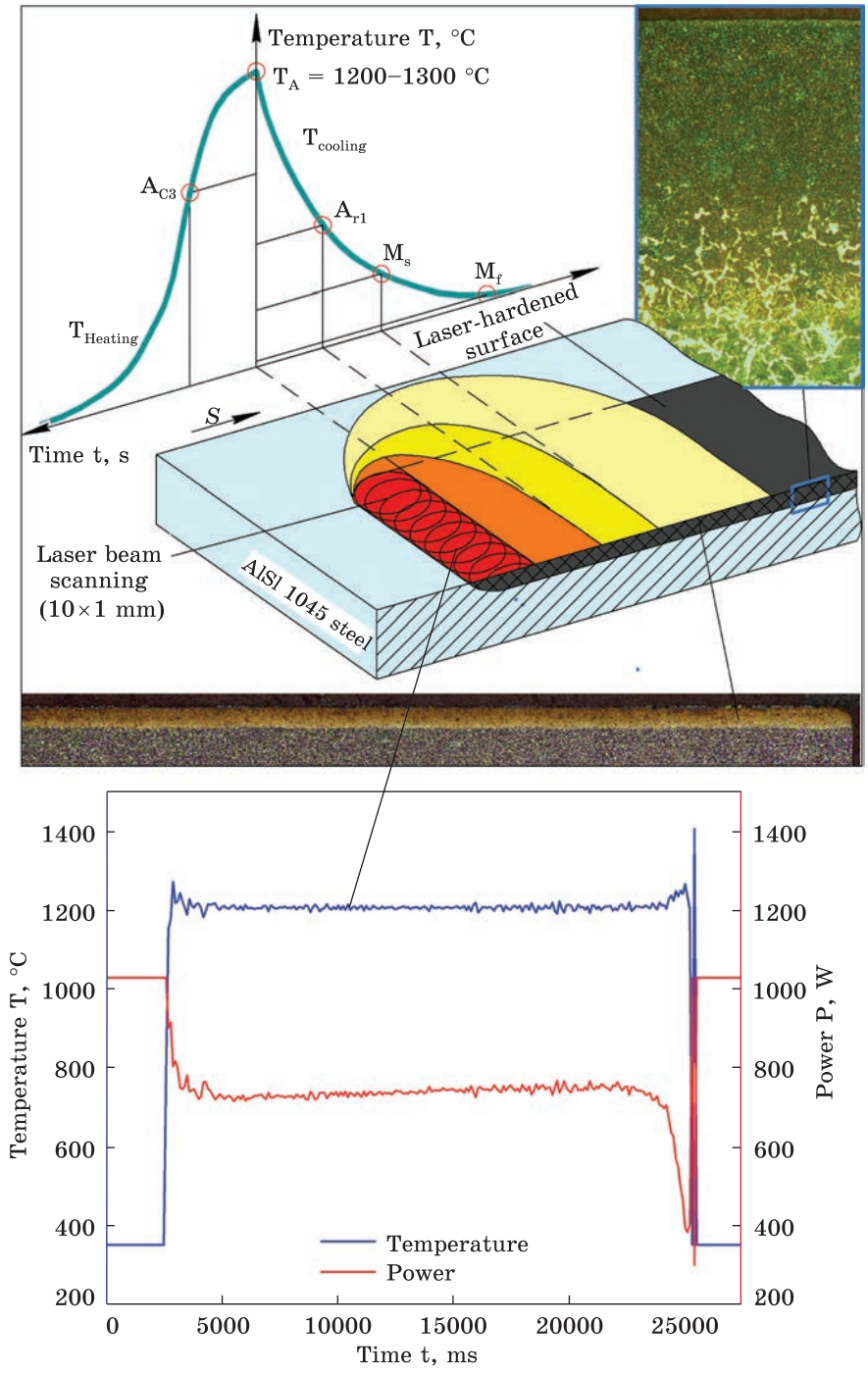

Fig. 1. Schematic illustration of the LHT process

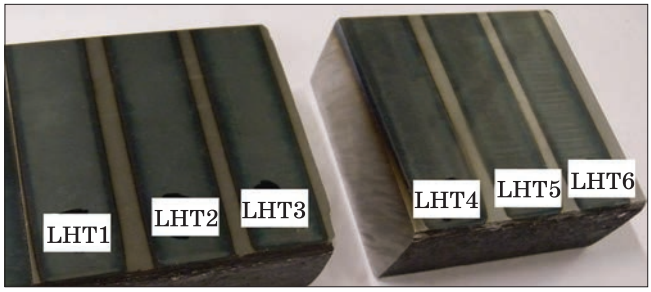

Fig. 2. The appearance of the LHT-processed samples

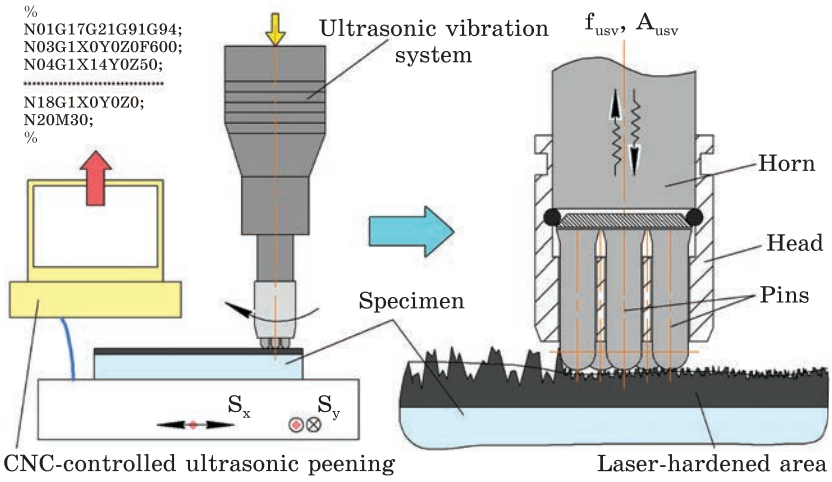

Fig. 3. Schematic illustration of the UIT process

Table 3. **Ultrasonic impact treatment parameters**

Regime abbreviation	Vibration amplitudes of ultrasonic horn, μm	Vibration frequency of the ultrasonic horn, kHz	Vibration frequency of pin impacts, kHz	Load of ultrasonic tool, N	Treatment duration, s
UIT1 UIT2	18	21.6	1	50	560 120

The visualization of the temperature–power control in the LHT3 mode is demonstrated below in Fig. 1.

The energy density of the laser beam at the LHT1–LHT6 modes was in the range of 31–105 kJ/cm^2, calculated by $E_{LHT} = P/(d \times S)$ [61], where P is the power of the laser beam [W]; d is the diameter of the laser beam [cm]; and S is the specimen feed rate of the treated surface [cm/min] (Table 2). The calculated values of the heat power density (W_{LHT}) of the laser beam for continuous energy supply ranged from 5.4×10^3 to $6.2 \times \times 10^3$ W/cm^2, determined by the absorbed power density of the scanning

laser beam [52]. The calculated laser-power density magnitudes confirm the absence of any surface melting of the studied material at the LHT parameters selected.

The ultrasonic impact treatment (UIT), also known as high-frequency mechanical impact (HFMI) treatment [109], of the LHT-processed steel samples, was carried out at room temperature by a multipin ultrasonic tool (Fig. 3) using a CNC milling machine, ultrasonic generator with a power output of 0.3 kW, ultrasonic oscillatory system, and electromotor [22, 46, 110].

The ultrasonic vibration system contained a piezoceramic transducer, a cylindrical waveguide horn, and a seven-pin impact head freely positioned at the horn tip (the pin diameter was 5 mm). The vibration amplitude and frequency of the ultrasonic horn were 21.6 kHz and 18 μm, respectively (Table 3). In the ultrasonic surface hardening and finishing process, the ultrasonic tool was pressed to the peened surface with a slight static load of 50 N while the impact head was forcedly rotated by means of an electric motor with a rotational speed of 76 rpm. It allowed severe plastic deformation of the surface by multiple sliding impacts with 1 ± 0.5 kHz. The UIT system is described in detail [50, 59, 111, 112, 113]. The UIT process lasted for 60 and 120 s provided relatively high coverage of the treated area (60×15 mm) (Table 3).

The energy of high-frequency impact by the pin was adopted to be equal to the kinetic energy of the ultrasonic horn tip, estimated by the formula [52]: $E_{UIT} = 2m\pi^2 f^2 A^2$, where m is the pin mass [g]; f and A are the vibration frequency [kHz] and amplitude [μm] of the ultrasonic horn, respectively. The impact energy during UIT was 8.95×10^{-3} mJ at the vibration frequency of the ultrasonic horn of 21.6 kHz and the vibration amplitude of the ultrasonic horn of 18 μm (Table 3). Additionally, total mechanical energy per the surface unit area accumulated during the UIT process was estimated by the equation [52]: $W_{UIT} = I_{UIT} f t_{UIT}$, where I_{UIT} is the mechanical intensity density [J/cm^2], f is the impact frequency [kHz]; and t_{UIT} is the UIT duration [s] (Table 3). The total mechanical energy values applied to the UIT-treated surface of the specimen by seven pins are in the range of 13–26 mJ/cm^2 for treatment duration of 60–120 s.

2.2. Characterization Techniques

The surface topography/texture in an area of 2.5×3 mm^2 of the specimens and the LHT + UIT-processed areas (the hardening depth, hardening width, and hardening angle) in the cross-section of the surface layers were studied using an optical 3*D* profilometer Leica DCM3D using a confocal scan mode (10XLD lens). The arithmetic mean roughness and waviness (*Ra* and *Wa*) profile parameters along the evaluation length were selected to evaluate the state of the unhardened and LHT+UIT-hardened surfaces. The

above-mentioned surface profile parameters were determined 6 times both in two orthogonal (X and Y) axes using a filter cut-off of 0.8 mm in each measurement in accordance with the international standard ISO 4287. The areal surface roughness parameters were also analysed using a standard ISO 25178. In particular, the arithmetic mean height *Sa* parameter was taken into account to evaluate area surface roughness.

The x-ray diffraction (XRD) analysis was carried out using a diffractometer (Rigaku Ultima IV) in CuK_α radiation with a graphite monochromator at a target voltage of 30 kV, current of 30 mA, and scanning speed of 2 o/min to determine the phase state in the subsurface layer (4–8 μm) [79]. To estimate the size D of crystallites/grains in the near-surface layer hardened by LHT+UIT, the full widths at half maximum (FWHM) of five reflections, which were assessed after their fitting by the pseudo-Voight function using Origin software, were analysed following the Scherrer's equation [110]: $\beta = (K\lambda/(D\cos\theta)) + \eta\tan\theta$, where D is the crystallite size, K is the constant ($K = 0.9$, assuming that all the grain sections are spherical), λ is the wavelength of x-ray radiation, θ is the angle of diffraction, η relates to the lattice microstrains, $\beta = (B^2 - b^2)^{1/2}$ is the physical broadening of the peak, B is the FWHM obtained from the modified layer, and b is the FWHM of instrumental broadening. Then, the lattice microstrains (η) and the crystallite size (D) values were evaluated as a slope and an intersection point of a linear function $\beta = f(\tan\theta)$ with the ordinate axis, which was obtained by the extrapolation of the experimental physical broadening β of the analysed reflections. The shifts of the angular positions of diffraction peaks (the changes in the lattice spacing d) in comparison with their positions in the diffraction pattern for the initial specimen (a reference lattice spacing in the initial state d_0) were accounted for the estimation of residual macrostresses using the following expression [79, 110]: $\sigma_1 + \sigma_2 = -E(d - d_0/(\upsilon d))$, where E is Young's modulus, ν is the Poisson's ratio, d is the measured lattice spacing in the LHT+UIT-hardened specimen.

Then, the LHT+UIT-processed specimens were mechanically cut, ground, and polished for cross-section microstructure examinations according to a standard metallographic procedure. The specimens were chemically etched by a 4% Nital reagent for 5 s to perform a light optical microscopy (LOM). The cross-section microstructure examinations were observed by a LOM microscope (Nikon Optiphot-100). Transmission electron microscopy (TEM) by a microscope (JEOL-CX-II 100) was also applied to characterize the microstructure of the subsurface layer in a range of 10–15 μm below the outmost surface of the specimens. The TEM foils were prepared from the central zone of the laser/ultrasonic track according to a standard procedure using a one-side polishing technique.

The HRC_5 hardness on the specimens' surfaces was measured using a universal digital hardness tester Computest SC at a load on an indenter of

5 kgf (49 N) for the dwell time of 3 s. In each case, six measurements were carried out in the central area of laser-ultrasonic tracks, and the average values were summarized. The scatter of the experimental data did not exceed 5%. The hardening intensity (u_h) values of the LHT + UIT-hardened specimens were evaluated by the ratio of the difference between the hardness values of the LHT + UIT-hardened (HRC_h) and the unhardened (HRC_{in}) surface according to the expression $u_h = (HRC_h - HRC_{in})/HRC_{in} \cdot 100\%$. Additionally, the ($HV_{0.3}/HV_{0.05}$) microhardness in the top surface layer (five measurements on the distance of ≈25 μm from the surface in the centre of the LHT + UIT-treated areas in the transverse direction of the heat-affected zone) and the microhardness depth measurements in the specimens' cross-sections in a central zone of the laser/ultrasonic tracks were registered using a FM800 digital tester at a load of 0.3 and 0.05 kgf on the Vickers indenter and dwell time of 12 s. An average of five measurements was taken at each depth to obtain the microhardness–depth profiles.

3. Surface Modification Outcomes

The combined application of both LHT and UIT results in several beneficial changes in the superficial microstructure characteristics of the middle-carbon steel 1045. First, the LHT process-induced surface oxidation is accompanied by the formation of a series of iron oxides (Fig. 4), which may play a protective role against corrosion and wear of the steel part surface in aggressive media.

Additionally, sequential LHT and UIT processes lead to the formation of the layered microstructure consisting of a deeper layer of LHT-induced fine martensitic structure (Figs. 7 and 8) and the top near-surface layer of nanocrystalline/ultrafine-grained structure produced by severe plastic deformation occurred at UIT (Figs. 6–8). The latter is often called a 'white layer' due to its hindered degradation in aggressive media [114, 115]. Nanocrystalline grains of martensite and/or carbon oversaturated ferrite are responsible for the enhanced resistance of this 'white layer' against corrosion and wear [52, 56, 79, 114, 116, 117].

The fragments of XRD patterns of the untreated and LHT-, LHT + UIT-processed specimens allow comparison of the appearance of numerous additional diffraction peaks from the iron oxides after the laser transformation hardening process and their removal after subsequent UIT. This observation correlates well with the data reported in Refs. [41, 46, 52, 56, 79, 118] regarding the formation and anticorrosion ability of the oxide layers (FeO and Fe_3O_4) on the LHT-processed and UIT + LHT-processed surfaces of AISI D2 and AISI 1045 steels. Since the iron oxide layers being fractured and scaled may exert a deteriorative influence on the wear process, a protective gas is often employed during the LHT process [82]. Evidently, the application of the finishing UIT process is also beneficial regarding

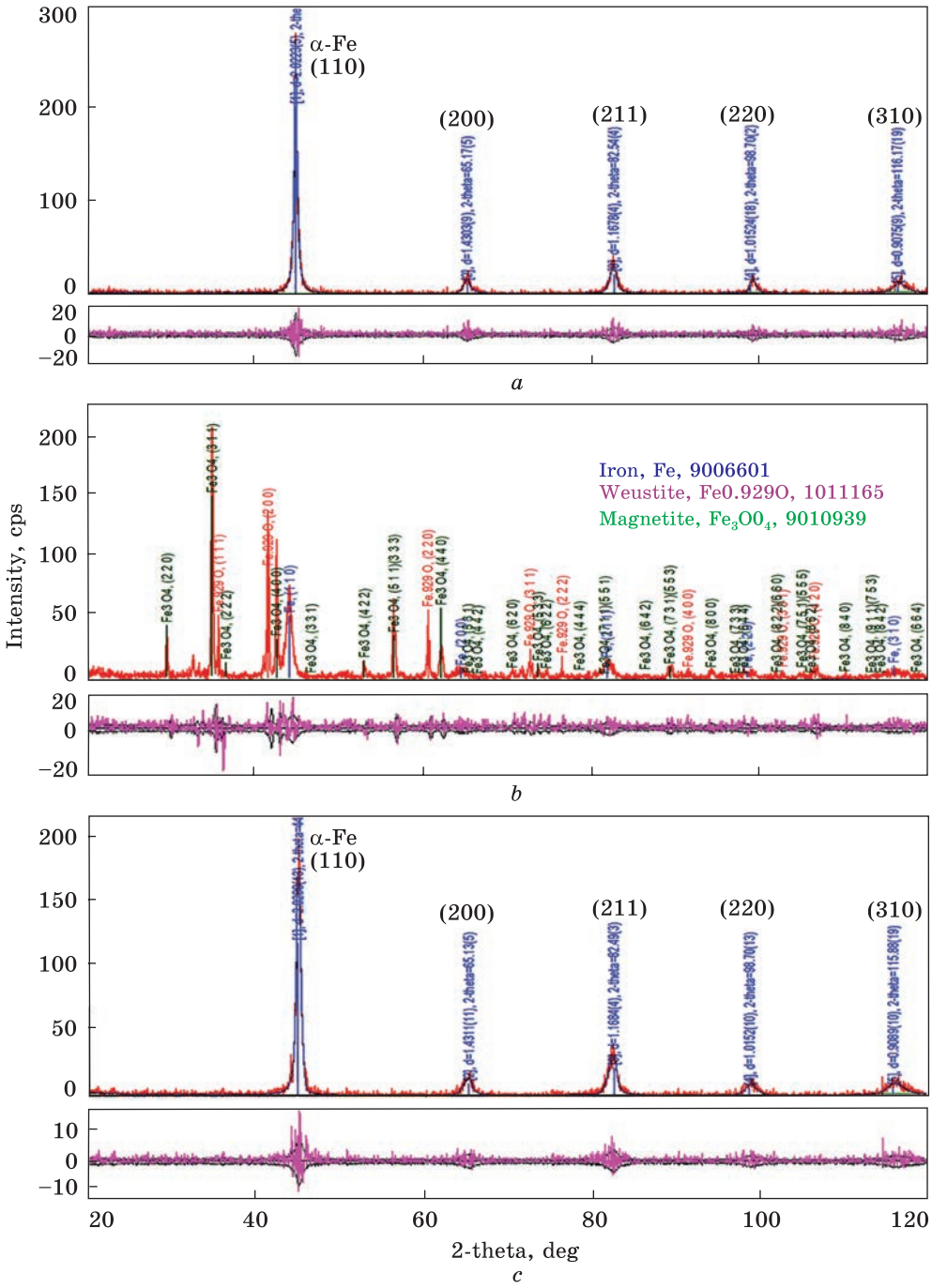

Fig. 4. Fragments of the XRD patterns of the unhardened (*a*), LHT-hardened (*b*), and combined LHT + UIT-hardened (*c*) AISI 1045 steel surface samples

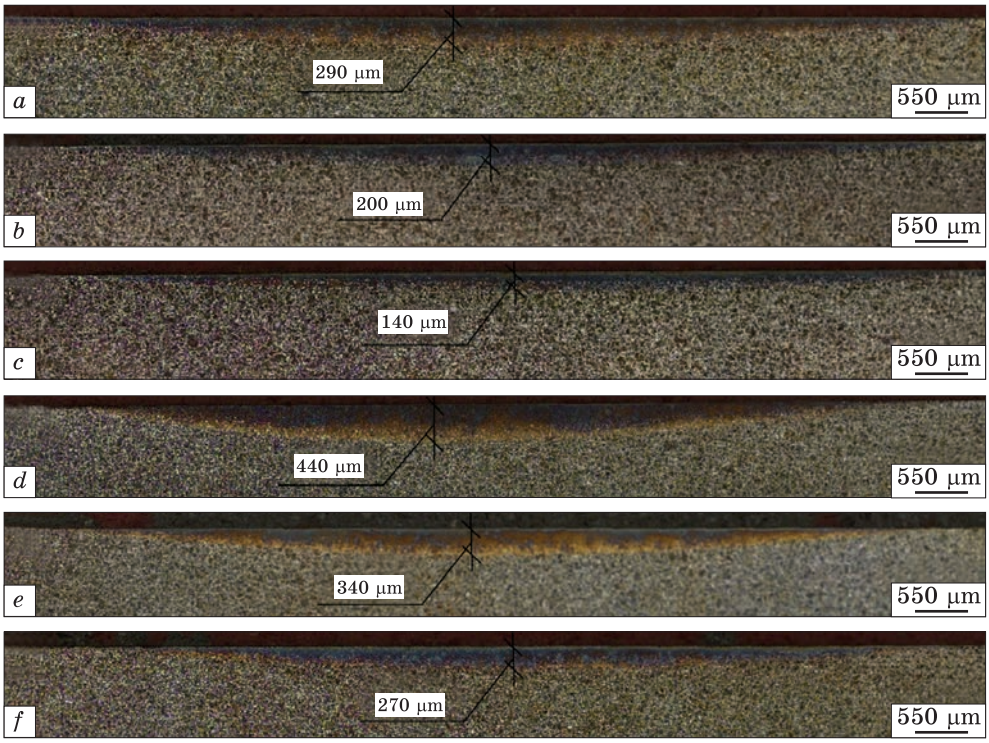

Fig. 5. Optical micrographs of the hardened zone in the AISI 1045 steel samples by LHT1 + UIT2 (*a*), LHT2 + UIT2 (*b*), LHT3 + UIT2 (*c*), LHT4 + UIT2 (*d*), LHT5 + UIT2 (*e*), and LHT6 + UIT2 (*f*) combined processing conditions

the removal of the lesser attached pieces of oxides and the improvement of wear resistance in the running-in stage of the wear process [56, 79].

The laser-ultrasonic hardened zones both on the surface and in the cross-section of the LHT-processed samples are given in Fig. 2 and Fig. 5, varying the heating temperature (1200 and 1300 °C) and LHT speed (40, 90, and 140 mm/min). Preliminary LHT results of the studied steel showed that the heating temperature of 900 °C at the sample feed rate of 40–140 mm/min (0.6–2.3 mm/s) did not provide the laser-hardened zones in the LHT-processed samples while the formed hardening depths (90–130 μm) at the heating temperature of 1050 °C [61] are not enough for structural steel parts that work in extreme conditions. This can be attributed to the ratio time–temperature above T_{AC3} is not enough, and the material austenitization has not been completed to increase the hardening depth of the surface layer with the appropriate near-surface hardness and grain structure refinement, avoiding the melting of the surface, it is required to study the effects of the laser phase transformation hardening process under the increased heating temperature (1200–1300 °C, Table 2) and LHT speed on the laser-hardened zone (Fig. 2).

3.1. Microstructural Features

The hardening depth, hardening width, and hardening angle were analysed in the samples' cross-section registered by the laser 3*D* profilometry (Fig. 6), which depends mainly on the heating temperature, workpiece feed rate, and laser beam spot. The LHT treatment with a fibre laser and scanning optics induced the hemispherical hardening zones with increased hardening depth in the centre of the laser track, assuming that the melting temperature was not reached at the surface. The final application of ultrasonic treatment does not lead to a change in the depth of hardening obtained by LHT.

The measured hardening width was 10.1 mm (LHT1), 10.0 mm (LHT2), 9.5 mm (LHT3), 10.5 mm (LHT4), 10.4 mm (LHT5), and 9.9 mm (LHT6), while the hardening angle was 6°15′ (LHT1), 5°18′ (LHT2), and 5°12′ (LHT3), 7°37′ (LHT4), 6°37′ (LHT5), and 6°10′ (LHT6). The geometrical dimensions of the laser-hardened zone, such as hardening width and hardening angle, were slightly increased after the LHT process at the increased heating temperature of 1300 °C (Fig. 6). The geometrical dimensions of

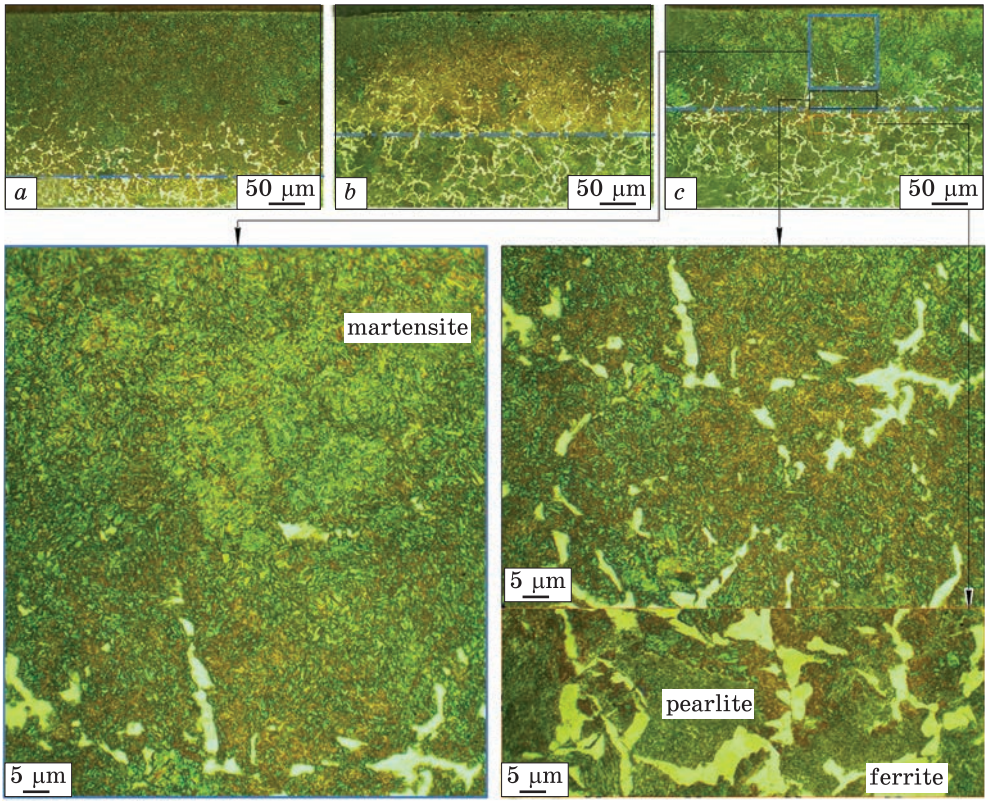

Fig. 6. Microstructure of the hardened zone in the combined LHT + UIT-processed AISI 1045 steel samples (α — ferrite, *P* — pearlite, α′ — martensite). Here, *a* — LHT4 + + UIT2; *b* — LHT5 + UIT2; *c* — LHT6 + UIT2

the laser-hardened zone are decreased with an increase in the sample feed rate affects the reduction in the time of the heating and cooling of the treated steel caused by the absorption of laser radiation by the surface layer. The depth of hardening also depends on the type of laser used (wavelength of laser radiation) [48, 119, 120].

Analysing the optical micrographs of the LHT+UIT-hardened zone in the AISI 1045 steel samples, it can be seen (Fig. 5) that the hardening depth was in a range of 140–290 μm for 1200 °C LHT and 270–440 μm for 1300 °C LHT using the fibre laser with the wavelength of 1.07 μm and scanning optics. The hardening depth was increased by 150–200% after the LHT treatment with an increased heating temperature (1300 °C). The hardened layer shape formed at high scanning speeds (1000 mm/s) is similar to the one that appears in the conventional laser hardening process, with a semi-elliptical shape with the maximum hardened thickness in the centre of the hardened track. The deeper hardened layers would be expected with higher heating temperature/laser power values. For instance, additional results showed that the hardening depth reached ≈500 μm at the heating temperature of 1350 °C, sample feed rate of 60 mm/min, and scanning speed of 1000 mm/s. In addition, it was observed that enhancement of the scanning speed resulted in an increase in the hardening depth. The maximum level of surface microhardness obtained by a 1 kW fibre laser system used was approximately 550 μm for AISI 1045 steel.

The typical layered heterogeneous microstructure formed in the near-surface layers of the LHT+UIT-processed medium-carbon steel samples is given in Fig. 6. In addition, Figure 6, *a*–*c* clearly shows the change in the microstructure-related hardening depth at a decrease in the sample feed rate for 1300 °C LHT. Compared to the volume structure of the medium-carbon steel consisting of a ferrite and pearlite mixture, the combined LHT+UIT-technology induced the layered hardening and grain structure refinement in the near-surface layers applying two-stage surface morphology modification by laser phase transformation followed by ultrasonic peening. At the first stage, the laser phase transformation hardening process by rapid heating to an austenitization temperature (1200–1300 °C) and subsequent fast cooling of the surface layer leads to the fine-grained martensitic microstructure formation in the near-surface layers containing ultrafine needle-like grains. It should also be noted that a complete transformation of excessive ferrite into austenite and saturation of former ferrite areas with carbon occurs in the upper layers heated to high temperatures [47, 79]. In the deeper layers, the saturation of the former ferrite areas with carbon does not occur since they are heated to lower temperatures (the cooling rate becomes lower than the critical one), and a troostite, troostite–ferrite, or ferrite nets are therefore formed [47, 68, 79, 121]. As seen in Fig. 6, *b* and Fig. 5, *c*, the LHT+UIT-affected zone is of ≈340 μm and ≈270 μm, respectively.

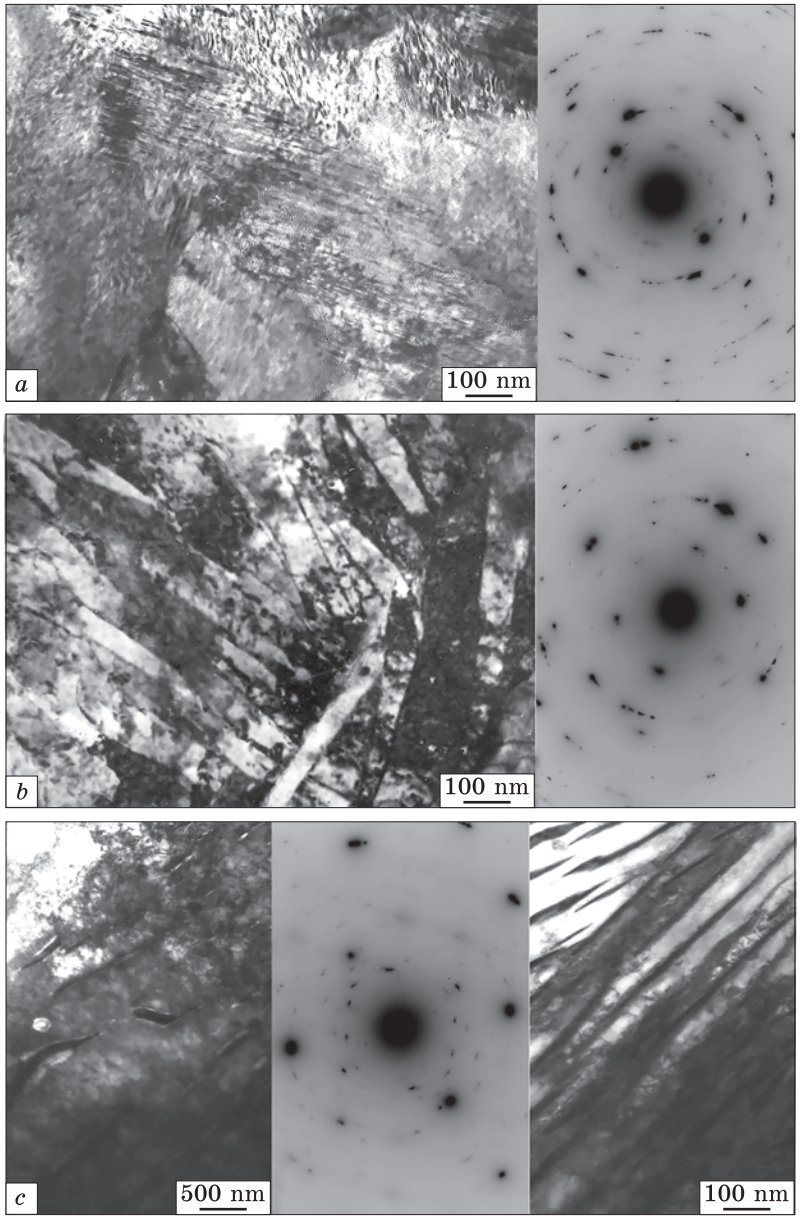

Fig. 7. TEM images and SAED patterns of the subsurface microstructure formed in AISI 1045 steel samples by the combined LHT + UIT treatment. Here, *a* — the outmost surface layer (≈ 10–15 μm deep); *b* — near-surface layer (50–100 μm deep); *c* and *d* — ferritic (*c*) and pearlitic (*d*) grains supplemented with electron diffraction pattern in the bulk material

In the second stage, the strain hardening induced by severe plastic deformation of the martensite ultrafine-elongated grains occurred in the near-surface layers during the UIT treatment appears the nanoequiaxed grains in the upper layers and nanoelongated grains in the deeper layers. The LHT+UIT microstructure observed in the top surface layer underwent the multipin UIT treatment and mainly contains the nanoequiaxed martensitic grain structure of inhibited etching (so-called 'white layer') in the near-surface layer [41, 79, 114, 116, 118, 122, 123].

TEM observations of the layered microstructure in the near-surface layers of the combined LHT+UIT-treated samples are shown in Fig. 7.

Figure 7, *a* shows the microstructure observed in the topmost surface layer (≅10 μm) underwent severe plastic deformation by UIT and was accompanied selected area electron diffraction (SAED) pattern. Mainly nanosize ferritic/martensitic grains (≈10–15 nm) of significant misorientations can be seen. In SAED, the reflexing spots of alpha iron are scattered both in radial and azimuthal directions that respectively indicate a high tetragonality of the α_T-Fe lattice of martensitic grains and the presence of the highly misoriented boundaries. This nanograined microstructure is responsible for XRD peaks broadening observed after LHT+UIT process (Fig. 8, *b*) and supports the highest hardness of top surface layer ≈11–12 GPa (*i.e.*, grain boundary hardening according to the Hall–Petch relation) (Fig. 9). Comparison of the broadening observed for samples underwent LHT with various scanning speed allows choosing an optimum LHT regime accounting the highest broadening related to the smallest grain/crystallite size and/or largest lattice microstrains (Fig. 8, *d*). Besides, the (310) peaks broadening for samples processed by LHT at 1300 °C are generally higher than that for samples processed at 1200 °C, which indicates both grain/crystallite refinement and increased lattice microstrains caused by strain-induced dislocations and carbon interstitials in martensitic/ferritic phase.

The deeper near-surface layer already contains the packets of the ultrafine microstructure needle-like martensitic grains of submicronic size, which were formed during quick heating/cooling at LHT (Fig. 7, *b*). It possesses slightly lower hardness (Figs. 9 and 11). The existence of martensitic and/or carbon supersaturated ferritic grains in both above-mentioned layers manifests itself by radially scattered diffraction spots in appropriate SAED patterns. This observation correlates with the splitting of the XRD (211) peaks related to the tetragonal b.c.t.-lattice of iron (Fig. 8, *a*), which is caused by carbon interstitials content in the iron lattice. It is important that some optimum scanning speed (90 mm/min) used at LHT regardless of the used temperature (1200 °C/1300 °C) can be observed accounting for the largest doublet splitting angular distance (Fig. 8, *c*). Several earlier studies reported similar correlations [41, 52, 56, 79]. However, the pseudo-tetragonal nature of the crystal lattice of martensite in carbon-containing steels is not the only explanation. It was recently pro-

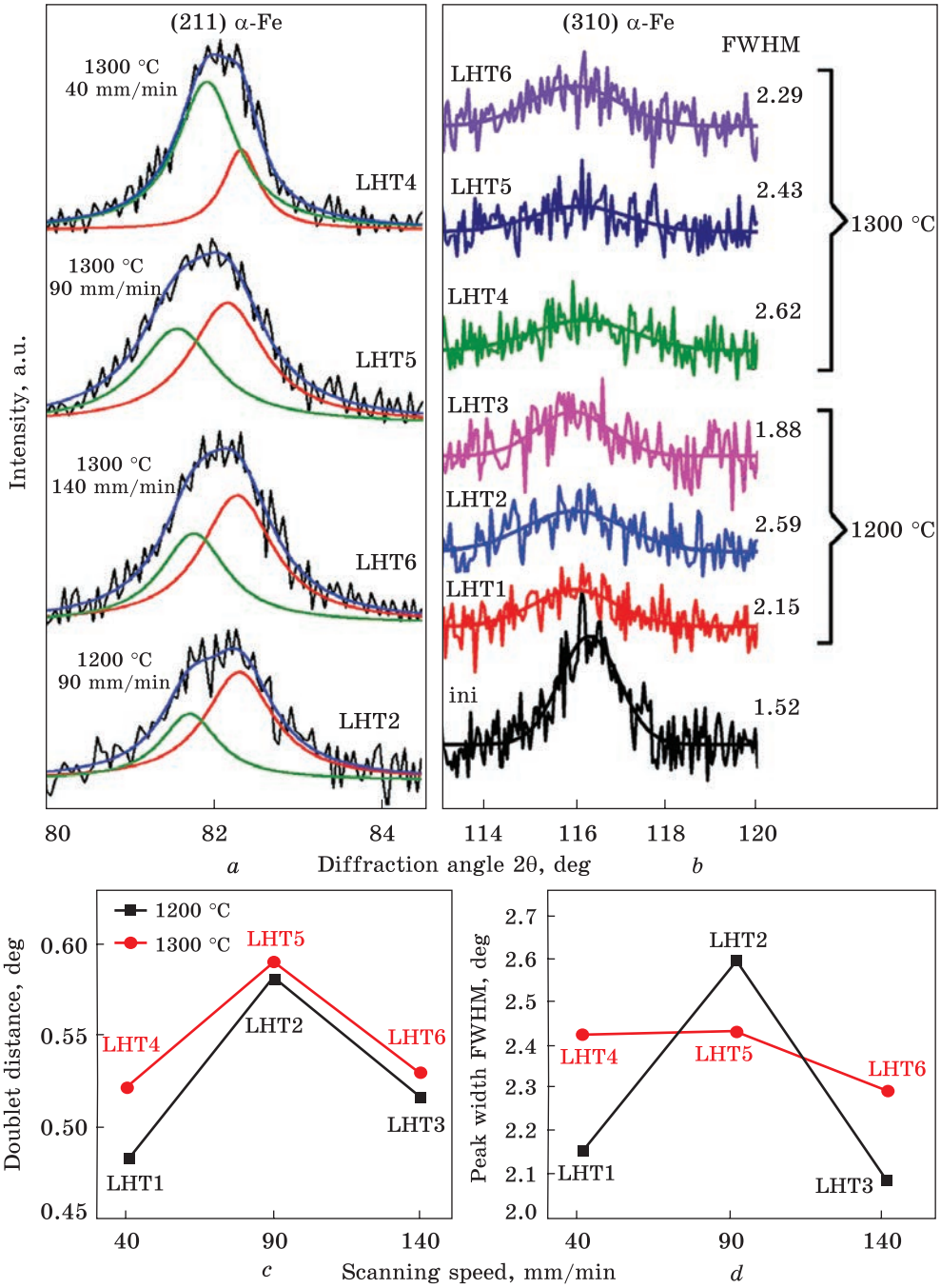

Fig. 8. Fragments of 211_{α} (*a*) and 310_{α} (*b*) diffraction maximums of the unhardened and combined LHT + UIT-hardened AISI 1045 steel samples, dependences of martensitic doublet splitting distance (*c*) and 310_{α} peak FWHM value (*d*) on the scanning speed at LHT

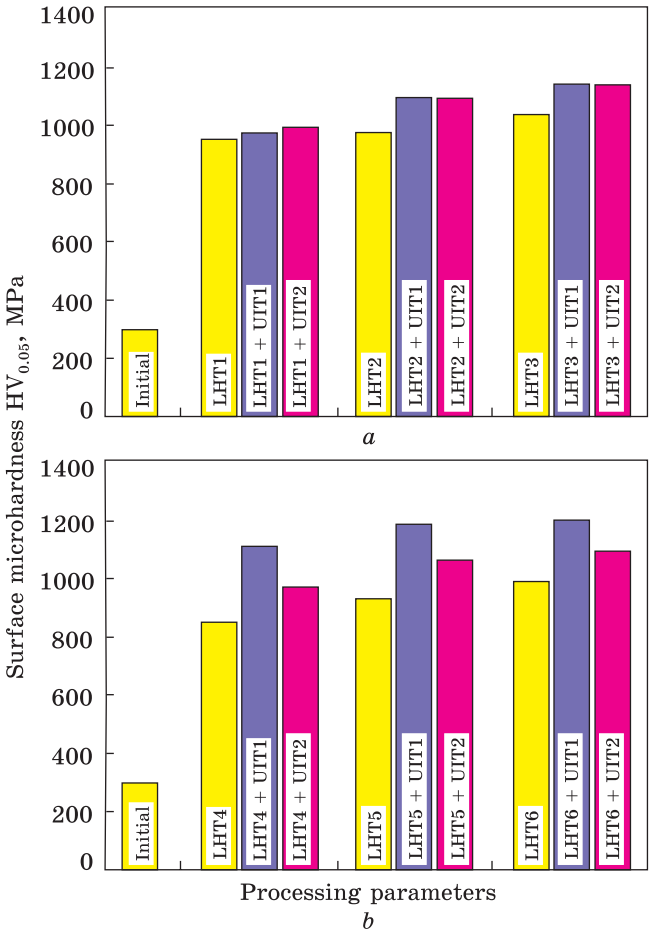

Fig. 9. Subsurface microhardness of the unprocessed, LHT-processed and LHT + UIT-processed AISI 1045 steel samples for (*a*) T = 1200 °C (LHT1, LHT2, LHT3) and (*b*) T = 1300 °C (LHT4, LHT5, LHT6)

posed that the periodic distortion of cube edges by the presence of carbon atoms is better reflected in the root-mean-square distortions of martensite lattice than by the value of doublet splitting of the corresponding x-ray reflections of the martensite crystal [124].

The microstructure of core material observed deeper than the laser-modified layer already contains two types of grains, *i.e.*, ferritic and pearlitic ones shown in Figs. 7, *c* and *d*, respectively. This microstructure naturally provides a lower microhardness of ≈3 GPa (Figs. 9 and 11).

The ultrasonic impact treatment process after LHT at both temperatures (1200 °C/1300 °C) leads to the formation of beneficial compressive residual stresses (–420–450 MPa) that manifest themselves as a shift of XRD peaks toward smaller diffraction angles.

The observed layered microstructure formed by the LHT + UIT process is shown to improve the operational properties and wear/anticorrosion resistance of the AISI 1045 steel [52, 62, 79]. Indeed, the increased

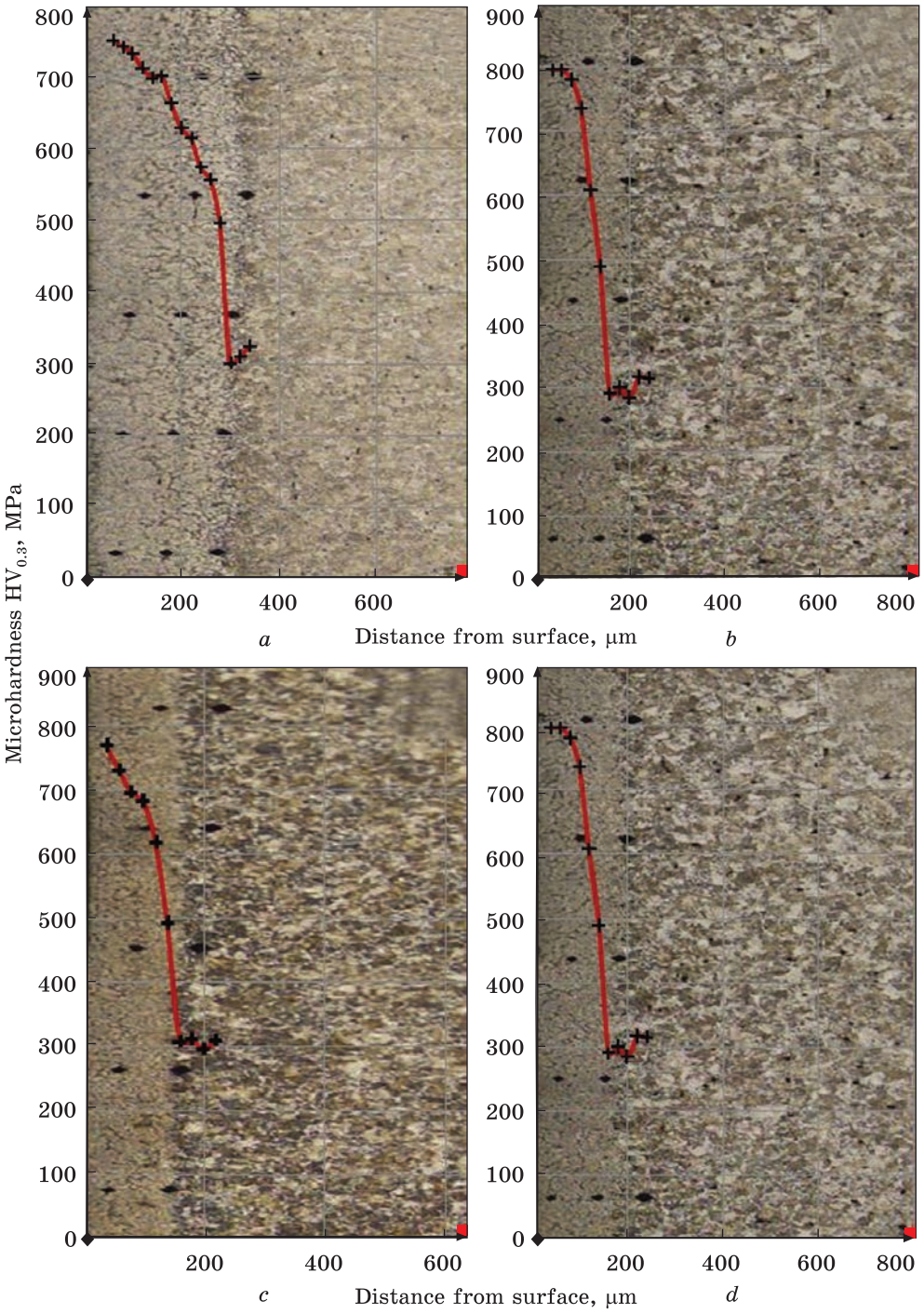

Fig. 10. Microhardness distribution ($HV_{0.3}$) along the depth in the near-surface layers of AISI 1045 steel samples processed by the combined LHT1 + UIT2 (*a*), LHT2 + UIT2 (*b*), LHT3+UIT1 (*c*), and LHT3+UIT2 (*d*) treatments

hardness of the nanoscale/ultrafine-grained outmost surface layer supported by hard enough ultrafine-grained ferritic/martensitic grains in the intermediated layer can provide high wear resistance according to the well-known Archard–Rabinowicz relation of inverse proportionality between wear and hardness [62, 79]. The observed nanograined structure in the top surface can also play the role of an anticorrosive protector for the AISI 1045 steel owing to the accelerated formation of the protective passive films [52].

3.2. Microhardness

Along with the near-surface phase and residual macrostress states, the structure-related surface hardness is also of particular importance for improving the operational properties of the structural steels.

The subsurface microhardness magnitudes and microhardness distribution along the depth in the near-surface layers of 1045 steel specimens processed by the single LHT and combined LHT + UIT treatment are presented in Figs. 9–11, varying the LHT speed and UIT duration (peening intensity). To identify the thin depths of hardening in the cross-section of the sample at UIT, the near-surface microhardness depth profiles were measured with a load on the indenter of 300 g (Fig. 10) and 50 g (Fig. 11).

The average subsurface microhardness (on the surface) for the unhardened specimens was around 300 $HV_{0.05}$ (Fig. 9). In general, the near-surface microhardness of 1045 steel increases with increasing laser processing speed irrespective of the heating temperature used. Additionally, it was noted for the lower specimen feed rate (40 mm/min) that the average surface hardness was about 950 $HV_{0.05}$ (1200 °C LHT) and 860 $HV_{0.05}$ (1300 °C LHT). This is because the higher the cooling rate, the lower the grain/crystallite size in the formed microstructure. As a consequence, the near-surface microhardness was achieved up to 950–1050 $HV_{0.05}$ at the specimen feed rate of 90–140 mm/min (Fig. 9).

The microhardness distribution along the depth in the near-surface layers (Figs. 10, 11) confirmed that the surface microhardness is slightly decreased at the heating temperature of 1300 °C and minimum speed of 40 mm/min during the LHT process. This can be attributed to some overheating, which can result in the appearance of an increased amount of residual austenite and larger grain size in the near-surface layer than those formed at higher LHT speeds (90–140 mm/min). Thus, an increase in the heating temperature and a decrease in the specimen feed rate causes a decrease in the cooling rate of the LHT-heated near-surface layers [46, 61]. Further decrease in the sample feed rate naturally results in the increase of the laser-affected zone dimensions, but it also leads to the diminution of the surface microhardness.

The hardening depths in the LHT+UIT-treated samples obtained from the depth profiles of near-surface microhardness (Fig. 11) are in good

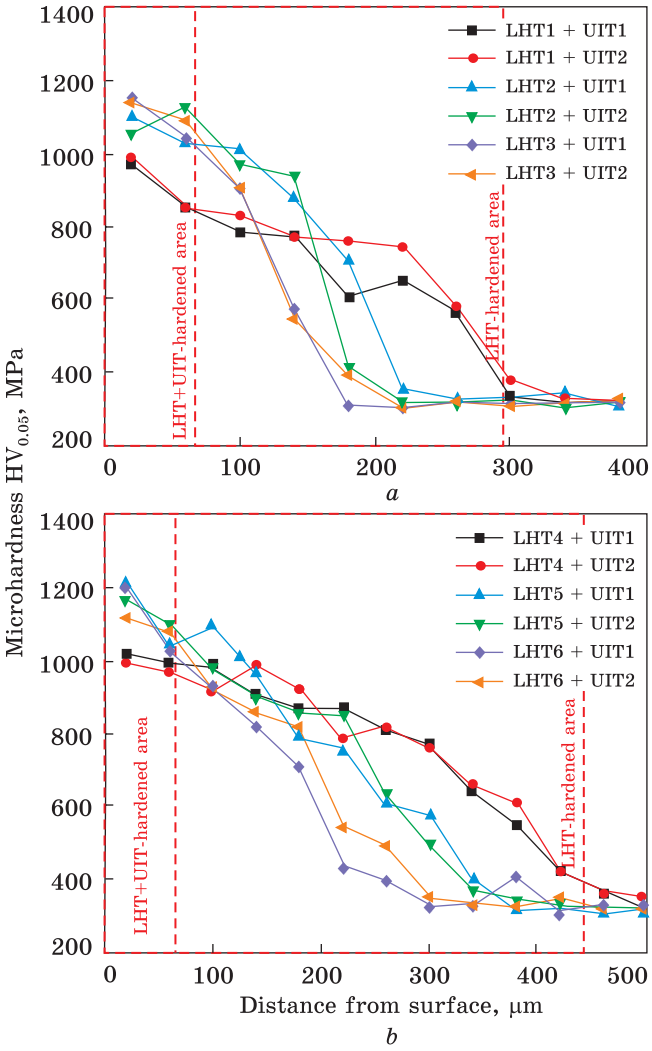

Fig. 11. Microhardness distribution ($HV_{0.3}$) along the depth in the near-surface layers of AISI 1045 steel samples processed by the combined LHT + UIT treatment for (*a*) T = 1200 °C (LHT1, LHT2, LHT3) and (*b*) T = 1300 °C (LHT4, LHT5, LHT6)

agreement with the determined hardening depths on the optical micrographs (Fig. 4).

Further application of the ultrasonic surface strengthening method for the LHT-processed samples contributes to the refinement and more uniform distribution of martensitic grains, as well as to an increase in the dislocation density, increasing the subsurface microhardness up to 970–1150 $HV_{0.05}$ (1200 °C LHT) (Fig. 11, *a*) and 980–1210 $HV_{0.05}$ (1300 °C LHT) at the depth of 60 μm (Fig. 11, *b*).

The microhardness results showed that the combined LHT+UIT treatment led to an almost triple increase in the near-surface microhardness (Fig. 9, Fig. 11) due to the fine-grained martensitic structure formation

(Fig. 7) and increasing the density of dislocations [52], irrespective of the conditions of surface formation by the laser phase transformation hardening process.

3.3. Surface Morphology

The surface microrelief obtained during combined laser-ultrasonic treatment is demonstrated in Figs. 12 and 13. The surface topography of 2.5×3.0 mm^2 was estimated using a non-contact profilometer. The surface microrelief coupled with the roughness and waviness parameters is known to play a major role in the corrosion and wear process during the running-in stage. In particular, Fig. 12 shows the surface topography after the laser hardening followed by ultrasonic peening at a temperature of 1200 °C, while Fig. 13 shows the surface topography at a temperature of 1300 °C.

In this work, the LHT treatment with a heating temperature control was applied to avoid any changes (melting of the surface even in microzones) in surface texture. The optimized UIT treatment of the LHT-processed AISI 1045 steel samples was implemented at higher vibration amplitude of the ultrasonic horn taking into account the significantly higher surface hardness of the LHT-treated surface of the test samples. The effects of the vibration amplitude of the ultrasonic horn (15–18 μm) and UIT duration (60–240 s) on surface texture and roughness parameters of the AISI 1045 steel are present in the work [61]. An increase in the UIT duration (>120 s) for the surface peening of the LHT-treated steels causes an increase in the surface roughness and waviness parameters [106].

Severe plastic deformation by the rotating multipin head leads to the formation of new surface microrelief (texture) on the LHT-processed AISI 1045 steel specimens (Figs. 12 and 13) instead of the surface-grinding marks in the initial specimens (Fig. 15). The microrelief obtained during combined LHT+UIT treatment is rather a smooth surface with wide dimples and peaks formed by the impact of the cylindrical steel pins in a diameter of 5 mm with a rounding radius of 5 mm. The mean width of the roughness profile elements is increased after LHT + UIT [41]. The surface flattening at the multipin UIT hardening and finishing process is associated with a high transversal constituent of load, which facilitates the sliding nature of multiple high-frequency impacts by the seven pins with high hardness.

It should also be noted that pre-treated surfaces by LHT with high hardness inhibit overstraining and formation of excessive grooves, peaks, and valleys during the UIT process. As a result, the LHT + UIT-formed surface microrelief is more flat and less wavy as compared to the surface microrelief induced by the single UIT treatment [61].

Thus, combined LHT + UIT treatment resulted in the formation of a smooth flattered microrelief on the surface of AISI 1045 carbon steel reg-

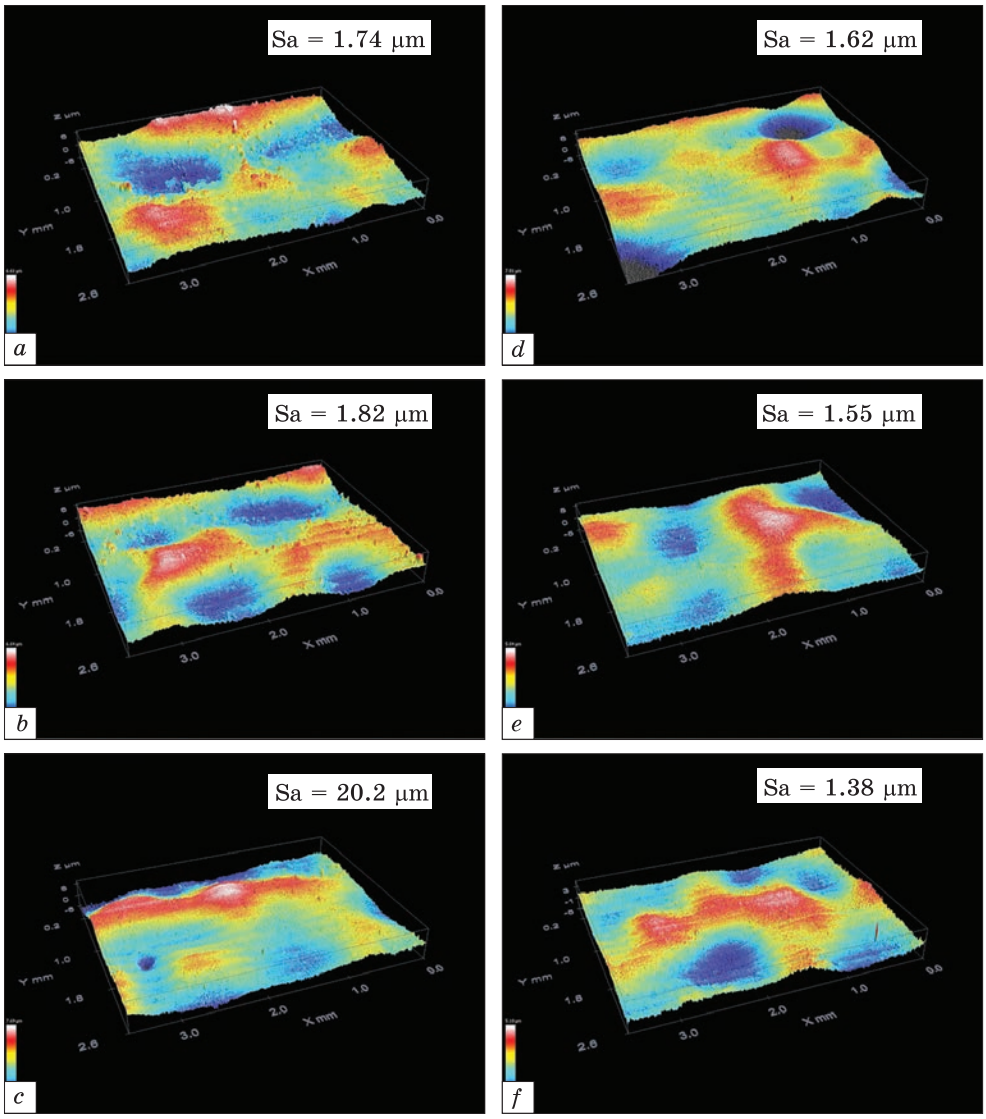

Fig. 12. Surface topography of the combined LHT12 + UIT1 (*a*), LHT2 + UIT1 (*b*), LHT3 + UIT1 (*c*), LHT1 + UIT2 (*d*), LHT2 + UIT2 (*e*), and LHT3 + UIT2-processed (*f*) AISI 1045 steel samples

istered by 3*D* laser microscopy. The application of the multipin UIT treatment using a rotating head promotes sliding with multiple high-frequency impacts of the pins, which causes flattening of microirregularities on the peened surface [43, 46, 50]. Such a smooth flattered microrelief with wide pockets formed by the LHT + UIT process will lead to reduced resistance to wear [79] and corrosion [51] of structural steels, as well as provide fa-

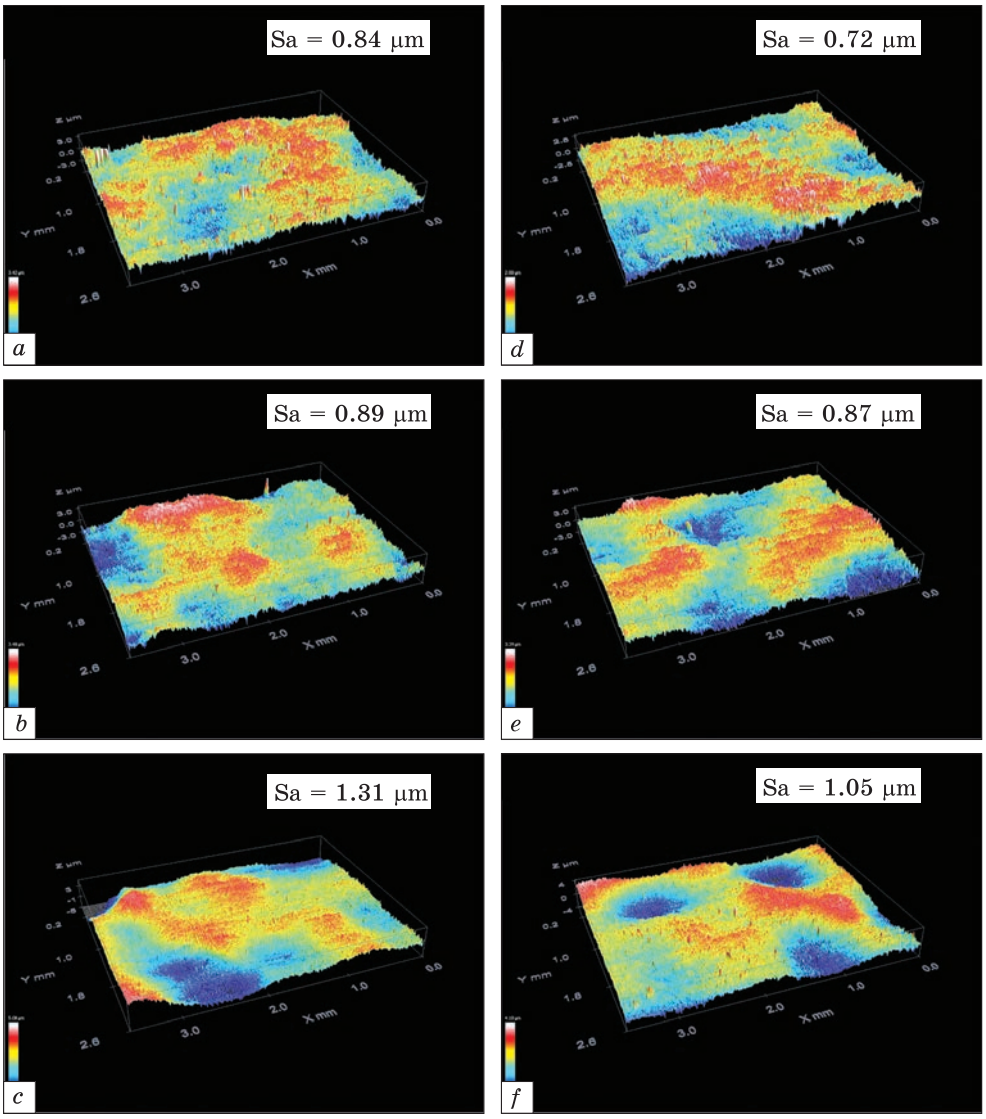

Fig. 13. Surface topography of the combined LHT4 + UIT1 (*a*), LHT5 + UIT1 (*b*), LHT6 + UIT1 (*c*), LHT4 + UIT2 (*d*), LHT5 + UIT2 (*e*), and LHT + UIT2-processed (*f*) AISI 1045 steel samples

vourable conditions to trap oil on the components' surface, and may be useful in various industrial applications.

The behaviour of the surface roughness parameter *Ra* and surface waviness parameter *Wa* (arithmetical mean height along the cut-off length of 0.8 mm for a roughness/waviness profile) after the LHT and LHT + UIT treatments is presented in Figs. 14–16.

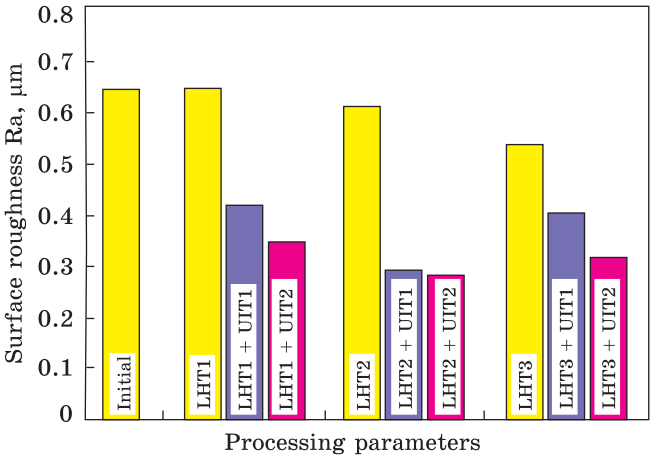

Fig. 14. Surface roughness of the initial, LHT-processed and LHT + UIT-processed AISI 1045 steel samples at the heating temperature of 1200 °C

The surface roughness of the single laser-processed AISI 1045 steel specimens is slightly decreased with specimen feed rate (Figs. 14 and 15). This tendency is observed both at the laser heating temperature of 1200 °C and 1300 °C. Compared to the initial state, the surface roughness almost does not change after laser surface hardening at the heating temperature of 1200 °C while the surface roughness deteriorates after LHT at a heating temperature of the treated sample of 1300 °C, regardless of the LHT speed used. This can be attributed to the formation of a thicker and non-uniform oxide layer at elevated LHT temperature of the studied steel (Fig. 15). The changes in surface roughness can occur because of surface oxidation when the surface of steel parts at the laser surface transformation hardening process is not protected by the shielding gases [41]. At the same time, the heating temperature values (even at the low LHT speed of 40 mm/min) applied at LHT did not lead to the melting of microasperities' peaks on the LHT-treated surface in this study. The absence of melting of the surface after the laser hardening can be observed in Fig. 5.

Applying multipin UIT tool for the surface treatment of the LHT-processed AISI 1045 steel specimens resulted in lower surface roughness due to the severe surface plastic strain (Fig. 14). It is of importance that compared to the different LHT-formed surface (Ra = 0.54–0.65 μm at 1200 °C and Ra = 1.24–2.66 μm at 1200 °C), the surface roughness parameters were reduced to the same level (Ra = 0.28–0.35 μm) using the combined LHT+UIT technique. By increasing the UIT duration, the surface roughness in the LHT + UIT-processed samples is slightly reduced.

At the same time, in contrast to the LHT treatment at 1200 °C, the UIT treatment after LHT caused a significant increase the surface waviness irrespective of the LHT speed used (Fig. 16). The Wa parameter was increased by UIT from 0.07–0.11 μm to 0.43–0.66 μm for UIT1 and 0.80–1.12 μm for UIT2. It was revealed that an increase in the UIT duration

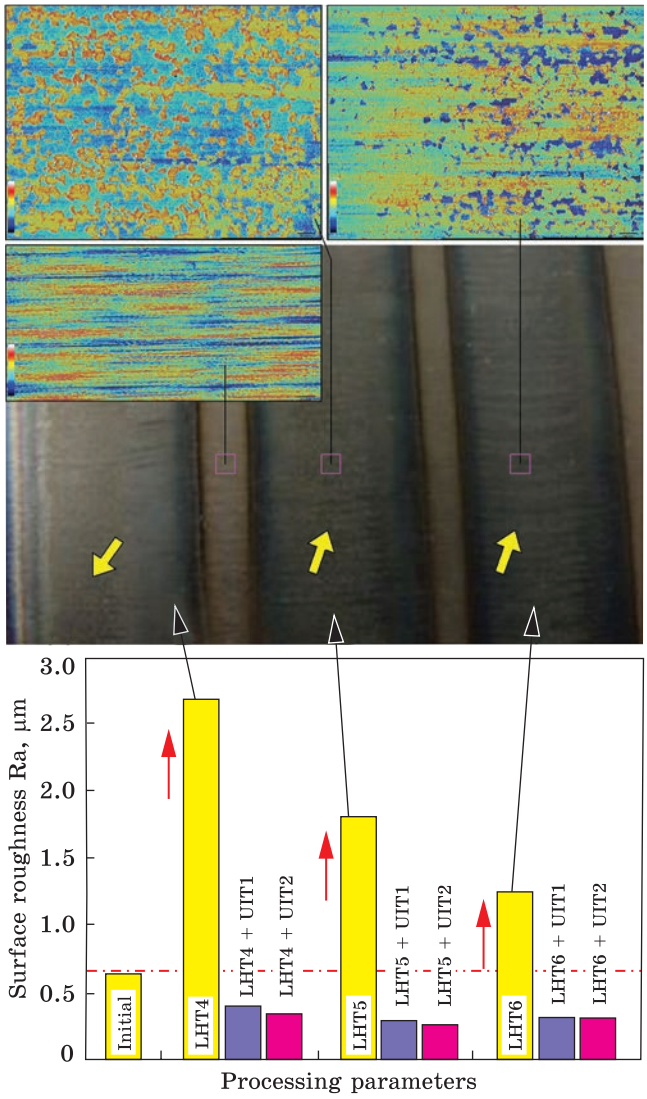

Fig. 15. Surface roughness of the initial, LHT-processed and LHT + UIT-processed AISI 1045 steel samples at the heating temperature of 1300 °C

leads to an increase in waviness on the processed surface (Fig. 16, *a*). However, when the formerly untreated surface has a higher waviness (roughness), as in the case of LHT at 1300 °C, a different trend is observed in Fig. 16, *b*.

The obtained results show that compared to the non-treated and LHT-hardened carbon steel parts, the LHT + UIT process leads to a significant change in the surface texture (Figs. 12 and 13), increasing the surface waviness (Fig. 16). Therefore, the increase the cost-effective use lubricants to enhance the wear and friction behaviours can be successfully achieved by the combined UIT + LHT technique.

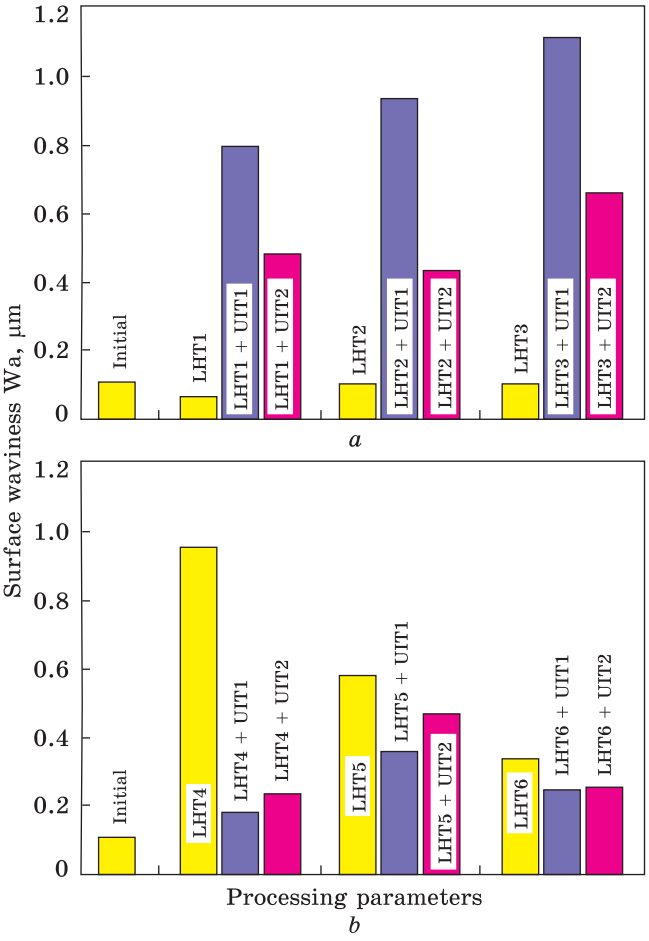

Fig. 16. Surface waviness of the initial, LHT-processed and LHT + UIT-processed AISI 1045 steel samples, where *a* — T = 1200 °C (LHT1, LHT2, LHT3) and *b* — T = 1300 °C (LHT4, LHT5, LHT6)

4. Discussion

4.1. Surface Hardening of AISI 1045 Steel by High-Power Laser Systems

Compared to traditional surface strengthening methods, the laser transformation hardening process offers numerous advantages, such as a lower risk of deformation and cracking, environmental friendliness, higher accuracy, and precision, as well as wider material suitability. These advantages make the LHT process suitable for the surface hardening of a variety of parts and products [48, 64].

The laser transformation hardening of steel products using commercial lasers is an effective method in which laser radiation of high-power density (10^3–10^4 W/cm^2) selectively heats the surface layer of the processed workpiece to high temperatures (usually slightly below the melting temperature), followed by rapid cooling. During the LHT process in continuous wave mode, the structural and phase transformations in iron–car-

bon alloys associated with rapid heating and cooling rates result in the formation of fine-grained near-surface microstructures of a martensitic nature and a high density of dislocations, increasing the mechanical properties and wear/corrosion resistance of the LHT-processed steel parts significantly [44, 47, 53, 57, 121, 125–127]. The LHT process refers to local methods of heat treatment using highly concentrated heating sources. The structural and phase transformations are a function of temperature, time, and thermal and physical properties of the LHT-treated surfaces [47, 57, 50]. As a consequence, the structural and phase transformations occur at several critical transformation points during the heating and cooling of steels, which play an important role in the creation of the mixed phases. The martensite phase formation in the LHT-processed surface areas confirmed the hardening of the steel [128].

The use of laser hardening systems depends on the material properties, dimensions, and complexity of the processed product, cost, and re-

Table 4. **LHT progress in surface hardening of AISI 1045 steel. Here, *P* is the laser power; *S* is the scanning speed; *PD* is the power density (W/cm^2); *T* is the heating temperature; *HD* is the hardening depth; *HW* is the hardening width**

Processing parameters	Laser type	Material	*HD*, mm	*HW*, mm	Hardness, GPa	Ref.
P = 1.3 kW S = 10 mm/s	CO_2 laser	AISI 1045	1	—	6.7	[66]
P = 1.8 kW S = 15 mm/s	CO_2 laser	AISI 1045	0.8	—	6.8	[68]
P is not assessed S = 25 mm/s	CO_2 laser	AISI 1045	0.7	3	6	[128]
$PD = 1\times10^4$–1.3×10^4 W/cm^2	Diode laser	AISI 1045	0.32	3.2	6	[128]
P = 0.72 kW S = 8 mm/s	Diode laser	AISI 1045	0.45	3.9	—	[119]
P = 0.76 kW S = 15 mm/s	Diode laser	AISI 1045	0.5	—	4	[129]
P = 1.1 kW S = 3.3 mm/s	Diode laser	AISI 1045	0.9	—	6.35	[130]
P = 0.9 kW S = 8.3 mm/s	Diode laser	AISI 1045	0.53	2.7	—	[131]
T = 1200–1300 °C S = 0.6–1.5 mm/s	Fibre laser	AISI 1045	0.2–0.44	10	8.6–9.5	This study
P = 1.2 kW S = 4.78 mm/s	Fibre laser	AISI 1045	1	3.3	6.6	[132]
P = 2.0 kW S = 12 mm/s	Disk laser	AISI 1045	1	10	7.8	[20]
P = 2.8 kW S = 70 mm/s	Disk laser	AISI 1045	1	1.1	6	[133]

quired operating conditions of the processed steel components. The laser surface hardening parameters (mainly laser power, scanning speed, and laser-beam spot) effects using the conventional CO_2 and Nd:YAG lasers on the features of structure formation in iron–carbon alloys were widely studied (Table 4). Works by Muthukumaran [45] and Orazi [66, 68] confirmed that the hardening depth (0.8–1 mm) and surface hardness (670–680 *HV*) were significantly enhanced in the studied AISI 1045 steel by the LHT process using the CO_2 laser. Li *et al.* [128] studied different infrared–red laser systems for the surface hardening of 8 mm thick steel specimens, confirming the benefit of a rectangular laser beam shape for the laser transformation hardening process. It is well known that the tempered martensite with inhomogeneous and low hardness is formed in the overlapping of laser tracks, which does not meet the minimum hardness requirements [43]. As a result, the hardened width with inhomogeneity of hardness formed by the CO_2 and Nd:YAG lasers with a circular laser beam spot is limited for critical applications.

Compact high-power diode lasers with more uniform power density are the heat sources to conduct directly the surface strengthening of steel parts and products. The LHT treatment using the diode/semiconductor lasers is effective for obtaining a uniform hardened layer during multiple overlapping tracks [128]. In addition, the wavelength of radiation of diode lasers (≈0.8 μm) makes it possible to significantly increase the absorption capacity of metals in comparison with the wavelength of the CO_2 laser (10.6 μm), reducing the dependence on surface roughness and cost of manufactured products [42]. The industrial diode lasers are more affordable compared to disk and CO_2 lasers. Works by Hagino [119], Lusquicos [129], Peeters [130], and Arai [131] showed that the surfaces hardened by a laser beam with a rectangular shape are characterized by the uniform depth of hardening and, accordingly, hardness distribution.

It should also be noted that the commercial high-efficiency fibre/disk lasers with a wavelength of 1.07 μm combined with advanced scanning optics are good tools for the surface hardening of structural steels, generating laser-irradiated track with customizable width [132, 133]. The LHT using the aligned heat sources (fibre and disk lasers) shows a controlled laser beam profile featuring reduced laser power density near the edge of oscillation [20, 53]. At the same time, the hardened surface up to 60–100 mm wide can be provided by high-power fibre and disk lasers [43].

Compared to the LHT process with a fixed defocused beam, both the properties of the surface layer and the hardening productivity by about 2 times will be provided using successfully aligned laser beams. Additionally, the use of the scanner-based laser transformation hardening system with programmable scanning parameters allows reducing energy costs by 25%, providing the specified geometry of the hardening areas [43, 45]. In this work, the laser surface transformation hardening of AISI 1045 steel

with the fibre laser, scanning optics, and PID temperature control induced the hardening depth of 0.2–0.44 mm and hardening width of ≈10 mm (Fig. 5), and hardness on the surface of 860–950 *HV* (Fig. 9, Table 4), avoiding the surface melting. To avoid surface oxidation at high temperatures during the LHT process, the shielding gas should be delivered into the processing areas, regardless of the type of laser used [132].

4.2. Correlation of Microstructure and Steel Properties Formed by Fibre Laser Hardening Process

The difference between laser phase transformation hardening of low-, medium-, and high-carbon steels or alloyed steels consists in their composition and mechanical properties [39, 48, 64, 128]. The hardenability of steels is increased with the increased content of alloying elements. The laser phase-transformation hardening effects using high-power fibre lasers on the hardening depth and surface hardness of various steels are summarized in Table 5.

Among iron–carbon alloys, low-carbon steels, also so-called mild steel, contain a small amount of carbon (the carbon percentage content is usually less than 0.3%). They may also contain small amounts of other chemical elements, such as copper and manganese. The laser heat treatment can increase the surface hardness and wear resistance of the low-carbon or low-alloy steels, making them suitable for applications in the automotive industry and tooling [134–136]. In general, the LTH method of steels results in a refined and hardened surface layer with a different microstructure from the base material. The authors of work [134] successfully hardened AISI 420 martensitic stainless steel (550 *HV*), achieving a high hardening depth (1 mm). Similarly, the works by Farshidianfar [135] and Qiu [136] reported that the steel austenitization (the carbon atoms in the metal lattice to rearrange) is more extensive and homogenous at the lower cooling and heating rates, which allows for more material to transform to martensite, obtaining higher hardness magnitudes. Oliveira *et al.* [137] demonstrated that the wear rate in non-hardened low-alloy steel is higher by three times compared to the LHT-hardened ones.

Medium-carbon steels contain a moderate amount of carbon (typically 0.3–0.6%). They may also contain other elements, such as manganese, silicon, and nickel. The LHT treatment can significantly increase the strength and wear resistance of medium-carbon steels, which are often used in the production of machine parts, where high strength is required [22, 72, 74, 132, 138–140]. Generally, the medium carbon steels hardened by fibre laser hardening systems contain a hardened surface layer with a layered microstructure consisting of fined-grained martensite with a high density of dislocations, while the HAZ zone may contain tempered martensite, bainite, and ferrite [48]. The initial state before the LHT process

affects the final structure of medium-carbon steel. The pre-hardening and tempering of AISI 1045 steel before laser processing induced the formation of the HAZ zone with a troostite structure of 300–400 *HV* (Fig. 11). Moreover, the microstructure is characterized the finer and more homogeneous as compared to the structure obtained by the Nd:YAG and CO_2 lasers [48, 128]. In this work, the formed structures (Figs. 6 and 7) by the fibre laser agree with the above-mentioned results.

The LHT application for the surface hardening of high-carbon (usually more than 0.6%) or high-alloy steels can be also applied to increase their wear resistance [20, 56, 80, 106] even though an increase in the steel carbon content above 0.6% sharply reduces the rate of hardness increase. The carbon diffusion in high-alloy steels is decreased as compared to the medium-carbon steels. As a result, the LHT parameters should be selected carefully to avoid the dissolution of the primary carbides and the formation of an increased amount of retained austenite. In particular, Raza *et al.* [141] studied the microstructural changes near the top, middle, and interfacial regions of the LHT-treated area of high-carbon steel (0.75% of C) with

Table 5. **LHT progress in surface hardening of steel parts using a fibre laser, where *P*, *S*, *T*, *HD*, and *HW* denote the same as in the previous table**

Processing parameters	Laser spot type	Material	*HD*, mm	*HW*, mm	Hardness, GPa	Ref.
P = 2 kW S = 5.8 mm/s	circular	AISI 420	1	4	5.5	[134]
P = 0.4 kW S = 8.3 mm/s	circular	AISI 1020	0.5	—	4.5	[135]
P = 1.4 kW S = 8 mm/s	circular	X15 steel	1.5	—	7.8	[136]
P = 0.6 kW S = 10 mm/s	circular	AISI 4130	0.24	1.46	3.9	[137]
P = 0.8 kW S = 20 mm/s	circular	AISI 4340	0.65	0.85	7.7	[72]
P = 2.5 kW S = 2 mm/s	circular	AISI 4340	0.95	—	6.4	[74]
P = 3 kW S = 15 mm/s	rectangle	AISI 4340	0.5	5.9	8.9	[138]
T = 1450 °C	rectangle	AISI 4140	1.1	25	6	[139]
P = 0.5–0.8 kW S = 1 mm/s	rectangle	X45CrSi9-3 steel	—	10	7.4	[140]
T = 1200–1300 °C S = 0.6–1.5 mm/s	rectangle	AISI 1045	0.2–0.44	10	8.6–9.5	This study
P = 1.2 kW S = 4.78 mm/s	circular	AISI 1045	1	3.3	6.6	[132]
P = 1.2 kW S = 6.6 mm/s	circular	High-carbon steel	0.34	2.4	9.3	[141]

and without surface melting using a 2 kW fibre laser. The results indicate that the melt zone generated fine-grained dendritic martensite microstructure and compressive residual macrostress, while the hardening zone induced relatively fine-grained microstructure with an increased amount of cementite and residual macrostress on the surface. The fragmented grain structure with grain boundaries fixed with fine secondary carbides is usually formed in high-alloy steels [46, 56], which has an additional positive effect on the wear resistance of the tool steels.

4.3. Laser-Assisted Mechanical Surface Hardening Effects on Surface Integrity of Steels

The results of this work indicate the beneficial effect of the fibre laser surface hardening process, in enhancing the surface hardness of AISI 1045 carbon steel (Table 5). At the same time, the reliability and durability of metal products are significantly obtained by both the structure/hardness and surface microrelief of structural steels. As a result, advanced combined/hybrid surface modification technologies are currently developed to provide better performance of critical steel products and parts [11, 28, 90, 92, 93, 98, 110–112, 142]. Compared to the combined thermochemical surface post-treatments [46, 79, 100, 103, 104], the thermomechanical surface modification processing (combined or hybrid strategy) resulted in the formation surface layer of mechanical properties and wear resistance of steels. In particular, the laser-assisted mechanical surface treatment

Table 6. Laser-assisted mechanical surface treatment methods for surface hardening and finishing of steel components, where *RS* is the subsurface residual macrostresses

Processing schemes	Material	*HD*, mm	Grain size, nm	Hardness, GPa	*Ra*, μm	*RS*, MPa	Ref.
LHT2 (fibre laser) + multipin UIT2	AISI 1045	0.20	21	11	0.26	−420	This study
LHT5 (fibre laser) + multipin UIT2	AISI 1045	0.34	26	10.7	0.26	−430	This study
LHT2 (fibre laser) + multipin UIT2 (hybrid process)	AISI 1045	0.25	10	11.5	0.2	—	[50]
Multipin UIT2 + LHT2 (fibre laser)	AISI 1045	0.40	40	10.6	0.43	−400	[79]
LHT (diode laser) + ultrasonic burnishing	25CrNi2MoV steel	0.32	25	6.7	0.35	−985	[102]
LHT (fibre laser) + ultrasonic burnishing (hybrid process)	AISI 300M	0.05	—	8.67	—	−955	[100]
LHT (Nd:YAG laser) + + burnishing (hybrid process)	AISI 4140	0.10	—	4.65	0.45	−600	[92]

(hybrid process) produced higher surface hardness and compressive residual macrostresses in the workpiece surface layer due to the temporary softening of the treated steel by the laser beam [50, 92, 100] (Table 6). As a result, the nanograined martensitic structures of considerable depth can be formed after the simultaneous action of the laser beam and the deformation tool located at a certain distance from the laser-beam action (UIT is applied during the workpiece cooling) [50]. However, hybrid methods of surface hardening and finishing have some limitations for processing steel products of complex shapes or small-size parts.

Application of the non-abrasive ultrasonic finishing methods combined with laser/plasma/electron-beam surface hardening techniques separately is the most promising development direction of surface post-treatment of the studied material. Compared to a single application of the LHT treatment, a more fragmented grain structure and a higher increase in the surface hardness and residual compressive macrostresses are obtained by the combination of laser surface hardening and ultrasonic burnishing and/or ultrasonic impact peening methods (Table 6).

The application of a combined method for surface hardening of AISI 1045 carbon steel, which consists of LHT+UIT or UIT+LHT is followed by the formation of gradient/layered structures (Figs. 5 and 6). Compared to the combined UIT+LHT treatment, the surface hardness is slightly higher after the combined LHT+UIT treatment due to the deformation-induced dissolution of retained cementite particles as well as the finer grain structure and white etching layers formation, providing a deeper compressive layer of the residual stress (Table 6) in the near-surface layer [25, 52, 79]. The main advantage of the combined UIT+LHT treatment over the combined LHT+UIT treatment is a higher hardening depth (Table 6) due to the laser heating followed by rapid cooling of the preliminary deformed ferrite grains saturated with carbon [52, 79].

Thus, the LHT+UIT-induced surface microrelief with low roughness parameters (Fig. 12–15), surface nanostructuring (Fig. 7), and residual compressive macrostresses on the surface can influence significantly such important operational properties as the wear, corrosion, fatigue, and strength of the structural steels, which largely determine the durability and operational life of the critical parts.

5. Conclusions

The ultrasonic impact treatment (high-frequency mechanical impact treatment) was applied to enhance the surface properties and microstructure of the AISI 1045 carbon steel processed by the fibre laser transformation hardening process.

The obtained results demonstrate that the combined LHT+UIT treatment is a feasible complex surface treatment for the quality improve-

ment of the structural steel components, including the surface microrelief (Ra = 0.28–0.35 μm), hardness (HV = 10–11 GPa), and residual stress (–420–450 MPa) characteristics.

The flattened surface microrelief formed by the combined LHT+UIT treatment can be effective in improving the final quality of the structural steel parts. The multipin UIT finishing after the LHT hardening process provides refinement of ultrafine martensitic grains fixed by fine grain-boundary cementite particles (≈10–15 nm), increasing the density of dislocations, and the virtual elimination of retained austenite in the near-surface layers, nanostructuring the subsurface layer that results in the formation of the protective layered hardened layer.

Moreover, the LHT+UIT treatment regime variation allows for obtaining the desirable mechanical properties and surface quality. The LHT treatment with the increased heating temperature (1300 °C) resulted in higher grain refinement and increased lattice microstrains caused by strain-induced dislocations and carbon interstitials in the martensitic phase as compared to the LHT at 1200 °C. The surface roughness and waviness parameters have the same trend of change after the application of the high-frequency mechanical-impact treatment regardless of the heating temperature used at the laser heat treatment. Increasing the peening intensity (UIT duration) of the LHT-hardened AISI 1045 steel samples leads to a decrease the surface roughness.

Acknowledgements. The paper contains results carried out within the framework of the joint Ukrainian–Czech R&D project for the period of 2021–2022 (agreements Nos. 0121U113829 and 0122U002389) and project of the National Academy of Sciences of Ukraine (agreement No. 0123U102368). Partial support by the European Union's HORIZON 2020 research and innovation programme under the Marie Sklodowska-Curie Grant (agreement No. 101034379) is also acknowledged. The authors are grateful to Prof. G.I. Prokopenko from the Physical Principles for Surface Engineering Department at the G.V. Kurdyumov Institute for Metal Physics of the N.A.S. of Ukraine for the support provided with the ultrasonic-impact treatment.

REFERENCES

1. J. Alcantara, D. de la Fuente, B. Chico, J. Simancas, I. Diaz, and M. Morcillo, *J. Manuf. Syst.*, **10**, No. 4: 406 (2017); https://doi.org/10.3390/ma10040406
2. W. Zhai, L. Bai, R. Zhou, X. Fan, G. Kang, Y. Liu, and K. Zhou, *Adv. Sci.*, **9**: 2003739 (2021); https://doi.org/10.1002/advs.202003739
3. M. Morcillo, I. Diaz, B. Chico, H. Cano, and D. de la Fuente, *Corros. Sci.*, **83**: 6–31 (2014); https://doi.org/10.1016/j.corsci.2014.03.006

4. L. Tan, L.L. Snead, and Y. Katoh, *J. Nucl. Mater.*, **478**: 42–49 (2016); https://doi.org/10.1016/j.jnucmat.2016.05.037
5. E. Mokhtari, A. Heidarpour, and F. Javidan, *J. Constr. Steel Res.*, **220**: 108840 (2024); https://doi.org/10.1016/j.jcsr.2024.108840
6. V.V. Tsyganov, R.E. Mokhnach, and S.P. Sheiko, *Steel Transl.*, **51**: 144–147 (2021); https://doi.org/10.3103/S096709122102011X
7. A. Mukherjee, C. Biswas, A. Majumder, M. Barik, and S. Banerjee, *Mater. Today*, **67**: 536–542 (2022); https://doi.org/10.1016/j.matpr.2022.07.257
8. A.R. Khalifeh, A.D. Banaraki, H.D. Manesh, and M.D. Banaraki, *Mater. Sci. Eng. A*, **712**: 232-239 (2018); https://doi.org/10.1016/j.msea.2017.11.025
9. N.-V. Nguyen, T.-H. Pham, and S.-E. Kim, *Mech. Mater.*, **137**: 103089 (2019); https://doi.org/10.1016/j.mechmat.2019.103089
10. J. Zheng, X. Zhou, Y. Yu, J. Wu, W. Ling, and H. Ma, *J. Clean. Prod.*, **253**: 119917 (2020); https://doi.org/10.1016/j.jclepro.2019.119917
11. S. Valkov, M. Ormanova, and P. Petrov, *Metals*, **10**: 1219 (2020); https://doi.org/10.3390/met10091219
12. R. Zenker, G. Sacher, A. Buchwalder, J. Liebich, A. Reiter, and R. Häßler, *Surf. Coat. Technol.*, **202**: 804–808 (2007); https://doi.org/10.1016/j.surfcoat.2007.05.089
13. K. Wang, Q. Ma, J. Xu, C. Liu, P. Wang, R. Chen, Y. Gao, and L. Li, *Mater. Today Commun.*, **31**: 103773 (2022); https://doi.org/10.1016/j.mtcomm.2022.103773
14. L.J. Yang, *J. Mater. Process. Technol.*, **113**: 521–526 (2001); https://doi.org/10.1016/S0924-0136(01)00583-0
15. D. Saha and S. Pal, *J. Mater. Eng. Perform.*, **25**: 2588–2599 (2015); https://doi.org/10.1007/s11665-019-04064-5
16. D. Guo, P. Zhang, Y. Jiang, C. Song, D.-Q. Tan, and D. Yu, *Tribol. Int.*, **169**: 107465 (2022); https://doi.org/10.1016/j.triboint.2022.107465
17. S. Guarino, M. Barletta, and A. Afilal, *J. Manuf. Process.*, **28**: 266–271 (2017); https://doi.org/10.1016/j.jmapro.2017.06.015
18. D.A. Lesyk, M. Hruska, B.N. Mordyuk, P. Kochmanski, and B. Powalka, *Lect. Notes Netw. Syst.*, **687**: 45–53 (2023); https://doi.org/10.1007/978-3-031-31066-9_5
19. V. Kostov, J. Gibmeier, and A. Wanner, *J. Mater. Process. Technol.*, **239**: 326–335 (2017); https://doi.org/10.1016/j.jmatprotec.2016.08.035
20. D.A. Lesyk, M. Hruska, O.O. Danyleiko, M. Honner, and V.V. Dzhemelinskyi, *Lect. Notes Netw. Syst.*, **472**: 30–36 (2022); https://doi.org/10.1007/978-3-031-05230-9_3
21. N. Maharjan, W. Zhou, Y. Zhou, Y. Guan, and N. Wu, *Surf. Coat. Technol.*, **366**: 311–320 (2019); https://doi.org/10.1016/j.surfcoat.2019.03.036
22. D.A. Lesyk, S. Martinez, B.N. Mordyuk, V.V. Dzhemelinskyi, and O.O. Danyleiko, *Lect. Notes Mech. Eng.*: 97–107 (2019); https://doi.org/10.1007/978-3-319-93587-4_11
23. E.M. Aragaw, E. Gärtner, and A. Schubert, *Procedia CIRP*, **94**: 914–918 (2020); https://doi.org/10.1016/j.procir.2020.09.072

24. M. Chemkhi, D. Retraint, A. Roos, C. Garnier, L. Waltz, C. Demangel, and G. Proust, *Surf. Coat. Technol.*, **221**: 191–195 (2013); http://dx.doi.org/10.1016/j.surfcoat.2013.01.047
25. D.A. Lesyk, W. Alnusirat, S. Martinez, B.N. Mordyuk, and V.V. Dzhemelinskyi, *Lect. Notes Mech. Eng.*: 313–322 (2022); https://doi.org/10.1007/978-3-030-91327-4_31
26. N. Maharjan, W. Zhou, Y. Zhou, Y. Guan, and N. Wu, *Surf. Coat. Technol.*, **366**: 311–320 (2019); https://doi.org/10.1016/j.surfcoat.2019.03.036
27. B. Wu, P. Wang, Y.-S. Pyoun, J. Zhang, and R. Murakami, *Surf. Coat. Technol.*, **213**: 271–277 (2012); https://doi.org/10.1016/j.surfcoat.2012.10.063
28. Y. Morisada, H. Fujii, T. Mizuno, G. Abe, T. Nagaoka, and M. Fukusumi, *Mater. Sci. Eng. A*, **505**: 157–162 (2009); https://doi.org/10.1016/j.msea.2008.11.006
29. U. Prisco, *Int. J. Adv. Manuf. Tech.*, **98**: 2619–2637 (2018); https://doi.org/10.1007/s00170-018-2412-0
30. M.K. Lee, G.H. Kim, K.H. Kim, and W.W. Kim, *J. Mater. Process. Technol.*, **176**: 140–145 (2006); https://doi.org/10.1016/j.jmatprotec.2006.03.119
31. Y. Xiang, D. Yu, X. Cao, Y. Liu, and J. Yao, *Proc. IMechE Part J: J. Eng. Tribol.*, **232**: 103773 (2017); https://doi.org/10.1177/1350650117729073
32. D. Guo, D. Yu, P. Zhang, Y. Duan, B. Zhang, Y. Zhong, and J. Qiu, *Surf. Coat. Technol.*, **394**: 125857 (2020); https://doi.org/10.1016/j.surfcoat.2020.125857
33. J. Xu, K. Wang, R. Zhang, Q.Guo, P. Wang, R. Chen, D. Zeng, F. Li, J. Guo, and L. Li, *Tribol. Int.*, **146**: 106032 (2020); https://doi.org/10.1016/j.triboint.2019.106032
34. A.T. Kanaev, A.V. Bogomolov, and T.E. Sarsembaeva, *Steel Transl.*, **42**: 544–547 (2012); https://doi.org/10.3103/S0967091212060083
35. P. Śliwiński, M.S. Węglowski, A.N. Wieczorek, and E. Skołek, *Surf. Eng.*, **40**, Iss. 3: 276–283 (2024); https://doi.org/10.1177/02670844241249728
36. Y. Fu, J. Hu, X. Shen, Y. Wang, and W. Zhao, *Nucl. Instrum. Methods Phys. Res. B*, **410**: 207–214 (2017); http://dx.doi.org/10.1016/j.nimb.2017.08.014
37. J. Yu, R. Wang, D. Wei, C. Meng, and H. Wu, *Nucl. Instrum. Methods Phys. Res. B*, **467**: 102–107 (2020); https://doi.org/10.1016/j.nimb.2020.02.006
38. D. Wei, X. Wang, R. Wang, and H. Cui, *Vacuum*, **149**: 118–123 (2018); https://doi.org/10.1016/j.vacuum.2017.12.032
39. P. Sentil Kumar, C. Jegadheesan, P. Somasundaram, S. Praveen Kumar, A. Vivek Anand, Ajit Pal Singh, and N. Jeyaprakash, State of art: review on laser surface hardening of alloy metals, *Mater. Today Proc.* (2023); https://doi.org/10.1016/j.matpr.2023.04.259
40. S. Guarino and G.S. Ponticelli, *Metals*, **7**: 447 (2017); https://doi.org/10.3390/met7100447
41. D.A. Lesyk, S. Martinez, B.M. Mordyuk, V.V. Dzhemelinskyi, A. Lamikiz, D. Grzesiak, A.V. Kotko, and W. Alnusirat, *MRS Adv.*, **8**: 988–995 (2023); https://doi.org/10.1557/s43580-023-00648-5

42. A.F. I. Idan, O. Akimov, L. Golovko, O. Goncharuk, and K. Kostyk, *Eastern-European J. Eenter. Technol.*, **80**: 447 (2016);
https://doi.org/10.15587/1729-4061.2016.65455
43. D.A. Lesyk, W. Alnusirat, S. Martinez, V.V. Dzhemelinskyi, B.N. Mordyuk, and A. Lamikiz, *Lasers Manuf. Mater. Process.*, **9**: 292–311 (2022);
https://doi.org/10.1007/s40516-022-00178-2
44. S. Martinez, D.A. Lesyk, A. Lamikiz, E. Ukar, and V.V. Dzhemelinskyi, *Phys. Procedia*, **83**: 1357–1366 (2016);
https://doi.org/10.1016/j.phpro.2016.08.143
45. G. Muthukumaran and P.D. Babu, *Braz. Soc. Mech. Sci. Eng.*, **43**: 103 (2021);
https://doi.org/10.1007/s40430-021-02854-4
46. D.A. Lesyk, S. Martinez, V.V. Dzhemelinskyi, A. Lamikiz, B.N. Mordyuk, and G.I. Prokopenko, *Surf. Coat. Technol.*, **278**: 108–120 (2015);
https://doi.org/10.1016/j.surfcoat.2015.07.049
47. S. Santhanakrishnan, F. Kong, and R. Kovacevic, *Int. J. Adv. Manuf. Technol.*, **64**: 219–238 (2013);
https://doi.org/10.1007/s00170-012-4029-z
48. M. Karamimoghadam, M. Rezayat, M. Moradi, A. Mateo, and G. Casalino, *Metals*, **14**: 339 (2024);
https://doi.org/10.3390/met14030339
49. B. Dinesh and P. Marimuthu, *Emerg. Mater. Res.*, **8**: 188–205 (2019);
https://doi.org/10.15587/1729-4061.2018.124031
50. V.V. Dzhemelinskyi, D.A. Lesyk, O.O. Goncharuk, and O.O. Danyleiko, *Eastern-European J. Eenter. Technol.*, **91**: 35–42 (2018);
https://doi.org/10.15587/1729-4061.2018.124031
51. P. Schußler, J. Damon, F. Muhl, S. Dietrich, and V. Schulze, *Comput. Mater. Sci.*, **221**: 112079 (2023);
https://doi.org/10.1016/j.surfcoat.2020.126275
52. D.A. Lesyk, B.N. Mordyuk, S. Martinez, M.O. Iefimov, V.V. Dzhemelinskyi, and A. Lamikiz, *Surf. Coat. Technol.*, **401**: 126275 (2020);
https://doi.org/10.1016/j.surfcoat.2020.126275
53. F. Qiu, J. Uusitalo, and V. Kujanpää, *Surf. Coat. Technol.*, **29**: 34–40 (2013);
https://doi.org/10.1179/1743294412Y.0000000049
54. M. Babic, G. Lesiuk, D. Marinkovic, and M. Cali, *Procedia Manuf.*, **55**: 253–259 (2021);
https://doi.org/10.1016/j.promfg.2021.10.036
55. H. Ki, S. So, and S. Kim, *J. Mater. Process. Technol.*, **214**: 2693–2705 (2014);
http://dx.doi.org/10.1016/j.jmatprotec.2014.06.013
56. D.A. Lesyk, S. Martinez, B.N. Mordyuk, V.V. Dzhemelinskyi, A. Lamikiz, G.I. Prokopenko, Yu.V. Milman, and K.E. Grinkevych, *Surf. Coat. Technol.*, **328**: 344–354 (2017);
https://doi.org/10.1016/j.surfcoat.2017.08.045
57. S. Santhanakrishnan and R. Kovacevic, *J. Mater. Process. Technol.*, **214**: 226–2271 (2012);
https://doi.org/10.1016/j.jmatprotec.2012.06.002
58. S. Oh and H. Ki, *Appl. Therm. Eng.*, **153**: 583–595 (2019);
https://doi.org/10.1016/j.applthermaleng.2019.01.050
59. D.A. Lesyk, S. Martinez, B.N. Mordyuk, V.V. Dzhemelinskyi, and O.O. Danyleiko, *Lect. Notes Mech. Eng.* (2020), p. 188–198;
https://doi.org/10.1007/978-3-030-22365-6_19
60. M.H. Farshidianfar, A. Khajepouhor, and A. Gerlich, *Surf. Coat. Technol.*, **315**: 326–334 (2017);

https://doi.org/10.1016/j.surfcoat.2017.02.055
61. D.A. Lesyk, S. Martinez, B.N. Mordyuk, V.V. Dzhemelinskyi, A. Lamikiz, and G.I. Prokopenko, *Opt. Laser Technol.*, **111**: 424–438 (2019); https://doi.org/10.1016/j.optlastec.2018.09.030
62. D.A. Lesyk, S. Martinez, B.N. Mordyuk, V.V. Dzhemelinskyi, and A. Lamikiz, *Lect. Notes Mech. Eng.* (2021), p. 62–72; https://doi.org/10.1007/978-3-030-77719-7_7
63. M.I.S. Ismail and Z. Taha, *Int. J. Technol.*, **1**: 79–87 (2014); https://doi.org/10.14716/ijtech.v5i1.156
64. Q. Yang, P. Zhang, Q. Lu, H. Yan, H. Shi, Z. Yu, T. Sun, R. Li, Q. Wang, Y. Wu, and J. Chen, *Opt. Laser Technol.*, **170**: 110202 (2024); https://doi.org/10.1016/j.optlastec.2023.110202
65. O.O. Danyleiko, V.V. Dzhemelinskyi, and D.A. Lesyk, *Eastern-European J. Enterprise Technol.*, **114**: 72–80 (2021); https://doi.org/10.15587/1729-4061.2021.247552
66. L. Orazi, A. Rota, and B. Reggiani, *Int. J. Mech. Mater. Eng.*, **16**: 2 (2021); https://doi.org/10.1186/s40712-020-00124-0
67. T.-P. Hung, H.-E. Shi, and J.-H. Kuang, *Materials. Eng.*, **11**: 1815 (2018); https://doi.org/10.3390/ma11101815
68. L. Orazi, A. Fortunato, G. Cuccolini, and G. Tani, *Appl. Surf. Sci.*, **256**: 1913–1919 (2010); https://doi.org/10.1016/j.apsusc.2009.10.037
69. X. Han, C. Li, Z. Liu, X. Chen, and S. Deng, *Opt. Laser Technol.*, **156**: 108613 (2022); https://doi.org/10.1016/j.optlastec.2022.108613
70. G. Muthukumaran and P.D. Babu, *Arab. J. Sci. Eng.*, **47**: 8785–8803 (2022); https://doi.org/10.1007/s13369-021-06350-8
71. 71. Z. Liu, J. Zhou, H. Wang, Q. Wang, Q. Liang, and Y. Li, *Int. J. Adv. Manuf. Technol.*, **122**: 499–512 (2022); https://doi.org/10.1007/s00170-022-09361-3
72. B. Tarchoun, A. El Ouafi, and A. Chebak, *J. Miner. Mater. Charact. Eng.*, **8**: 9–26 (2020); https://doi.org/10.4236/jmmce.2020.82002
73. C. Chen, X. Zeng, Q. Wang, G. Lian, X. Huang, and Y. Wang, *Opt. Laser Technol.*, **124**: 105976 (2020); https://doi.org/10.14716/ijtech.v5i1.156
74. N. Barka, S.S. Karganroudi, R. Fakir, P. Thibeault, and V.B.F. Kemda, *Coatings*, **10**: 342 (2020); https://doi.org/10.3390/coatings10040342
75. F. Frerichs, Y. Lu, T. Lubben, and T. Radel, *Opt. Laser Technol.*, **11**: 465 (2021); https://doi.org/10.3390/met11030465
76. V.V. Dzhemelinskyi, M. Hruska, B.N. Mordyuk, D. Grochala, and D.A. Lesyk, *Lect. Notes Netw. Syst.* (2024), p. 178–187; https://doi.org/10.1007/978-3-031-61797-3_15
77. Y. Lu, L.C. Ehle, S. Richter, and T. Radel, *Surf. Coat. Technol.*, **421**: 127434 (2021); https://doi.org/10.1016/j.surfcoat.2021.127434
78. M. Babic, J. Balic, M. Milfelner, I. Belic, P. Kokol, M. Zorman, and P. Panjan, *Adv. Prod. Eng. Manag.*, **8**: 25–32 (2013); https://doi.org/10.14743/apem2013.1.150
79. D.A. Lesyk, S. Martinez, B.N. Mordyuk, V.V. Dzhemelinskyi, A. Lamikiz, G.I. Prokopenko, M.O. Iefimov, and K.E. Grinkevych, *Wear*, **462–463**: 203494 (2020);

https://doi.org/10.1016/j.wear.2020.203494
80. D.A. Lesyk, S. Martinez, B.N. Mordyuk, V.V. Dzhemelinskyi, A. Lamikiz, G.I. Prokopenko, K.E. Grinkevych, and I.V. Tkachenko, *J. Mater. Eng. Perform.*, **27**: 764–776 (2018);
https://doi.org/10.1007/s11665-017-3107-7
81. S. Roy, J. Zhao, P. Shrotriya, and S. Sundararajan, *Tribol. Int.*, **112**: 94–102 (2017);
https://doi.org/10.1016/j.triboint.2017.03.036
82. O. Yazici and S. Yilmaz, *Tribol. Int.*, **119**: 222–229 (2018);
https://doi.org/10.1016/j.triboint.2017.11.006
83. S. Lei, Q.K. Liu, Y.P. Liu, and H. Li, *Mater. Sci. Forum*, **628–629**: 697–702 (2009);
https://doi.org/10.4028/www.scientific.net/MSF.628-629.697
84. D.I. Pantelis, E. Bouyiouri, N. Kouloumbi, P. Vassiliou, and A. Koutsomichalis, *Surf. Coat. Technol.*, **298**: 125–134 (2002);
https://doi.org/10.1016/j.triboint.2017.03.036
85. R. Sola, R. Giovanardi, P. Veronesi, and G. Poli, *Met. Sci. Heat Treat.*, **54**: 644–647 (2012);
https://doi.org/10.1007/s11041-013-9564-1
86. G.S. Ponticelli, S. Guarino, and O. Giannini, *Appl. Sci.*, **10**: 1401 (2020);
https://doi.org/10.3390/app10041401
87. A. Buchwalder and R. Zenker, *Surf. Coat. Technol.*, **375**: 920–932 (2019);
https://doi.org/10.1016/j.surfcoat.2019.07.084
88. D. Heinze, A. Buchwalder, A. Jung, A. Weidner, C. Segel, A. Muller, R. Zenker, and H. Biermann, *Metall. Mater. Trans. A*, **47**: 123–138 (2016);
https://doi.org/10.1007/s11661-015-3017-y
89. R. Zenker, A. Buchwalder, K. Ruthrich, W. Griesbach, and K. Nagel, and H. Biermann, *Surf. Coat. Technol.*, **236**: 58–62 (2013);
https://doi.org/10.1016/j.surfcoat.2013.06.118
90. M. Ormanova, P. Petrov, and D. Kovacheva, *Vacuum*, **135**: 7–12 (2017);
https://doi.org/10.1016/j.vacuum.2016.10.022
91. Y. Morisada, H. Fujii, T. Mizuno, G. Abe, T. Nagaoka, and M. Fukusumi, *Mater. Sci. Eng. A*, **505**: 157–162 (2009);
https://doi.org/10.1016/j.msea.2008.11.006
92. Y. Tian and Y.C. Shin, *Int. J. Mach. Tools Manuf.*, **47**: 14–22 (2007); https://doi.org/10.1016/j.ijmachtools.2006.03.002
93. J. Radziejewska and S.J. Skrzypek, *J. Mater. Process. Technol.*, **209**: 2047–2056 (2009);
https://doi.org/10.1016/j.jmatprotec.2008.04.067
94. J. Radziejewska, *Mater. Des.*, **32**: 5073–5081 (2011);
https://doi.org/10.1016/j.matdes.2011.06.035
95. Z. Wang, C. Jiang, X. Gan, Y. Chen, and V. Ji, *Int. J. Fatigue*, **33**: 549–556 (2011);
https://doi.org/10.1016/j.ijfatigue.2010.10.010
96. Z. Wang, C. Jiang, X. Gan, and Y. Chen, *Appl. Surf. Sci.*, **257**: 1154–1160 (2010);
https://doi.org/10.1016/j.apsusc.2010.07.015
97. Z. Wang, Y. Chen, and C. Jiang, *Appl. Surf. Sci.*, **257**: 9830–9835 (2011);
https://doi.org/10.1016/j.apsusc.2011.06.032
98. J. Liu, C. Ye, and Y. Dong, *Adv. Ind. Manuf. Eng.*, **2**: 100006 (2021);
https://doi.org/10.1016/j.aime.2020.100006
99. G.V. Inamke, L. Pellone, J. Ning, and Y.C. Shin, *Int. J. Adv. Manuf. Technol.*, **104**: 907–919 (2019);
https://doi.org/10.1007/s00170-019-03868-y

100. W. Zhao, D. Liu, J. Liu, X.H. Zhang, H. Zhang, R. Zhang, Y. Dong, and C. Ye, *Adv. Ind. Manuf. Eng.*, **23**: 2001203 (2021); https://doi.org/10.1002/adem.202001203
101. S.A. Ojo, K. Manigandan, G.N. Morscher, and A.L. Gyekenyesi, *J. Mater. Eng. Perform.*, **33**: 10345–10359 (2024); https://doi.org/10.1007/s11665-024-09323-8
102. X. Hu, S. Qu, Z. Chen, P. Zhang, Z. Lu, F. Lai, C. Duan, and X. Li, *Opt. Laser Technol.*, **155**: 108370 (2022); https://doi.org/10.1016/j.optlastec.2022.108370
103. X. Hu, H. Guan, Z. Chen, X. He, M. Wang, and S. Qu, *Mater. Sci. Eng. A*, **862**: 144495 (2023); https://doi.org/10.1016/j.msea.2022.144495
104. J. Liu, S. Suslov, Z. Ren, Y. Dong, and C. Ye, *Int. J. Mach. Tools Manuf.*, **136**: 19–33 (2019); https://doi.org/10.1016/j.ijmachtools.2018.09.005
105. D.A. Lesyk, V.V. Dzhemelinskyi, B.M. Mordyuk, S. Martinez, P.V. Kondrashev, D. Grzesiak, Yu.V. Klyuchnikov, and A. Lamikiz, *Eastern-European J. Enter. Technol.*, **122**: 17–26 (2023); https://doi.org/10.15587/1729-4061.2023.277252
106. D.A. Lesyk, B.N. Mordyuk, S. Martinez, V.V. Dzhemelinskyi, and A. Lamikiz, *Lect. Notes Mech. Eng.* (2004), p. 296–306; https://doi.org/10.1007/978-3-031-42778-7_27
107. G. Singh, *Mater. Today Proc.*, **37**: 2266–2268 (2021); https://doi.org/10.1016/j.matpr.2020.07.702
108. S. Singh, S. Samir, K. Kumar, and S. Thapa, *Mater. Today Proc.*, **45**: 5097–5101 (2021); https://doi.org/10.1016/j.matpr.2021.01.590
109. V.V. Knysh, B.N. Mordyuk, S.O. Solovei, P.Y. Volosevich, M.A. Skoryk, and D.A. Lesyk, *Int. J. Fatigue*, **177**: 107926 (2023); https://doi.org/10.1016/j.ijfatigue.2023.107926
110. D.A. Lesyk, B.N. Mordyuk, V.V. Dzhemelinskyi, S.M. Voloshko, and A.P. Burmak, *J. Mater. Eng. Perform.*, **31**: 8567–8584 (2022); https://doi.org/10.1007/s11665-022-06861-x
111. D.A. Lesyk, W. Alnusirat, V.V. Dzhemelinskyi, A.P. Burmak, B.N. Mordyuk, *Lect. Notes Mech. Eng.* (2022), p. 435–444; https://doi.org/10.1007/978-3-031-06025-0_43
112. D.A. Lesyk, H. Soyama, B.N. Mordyuk, O. Stamann, and V.V. Dzhemelinskyi, *Metallofiz. Noveishie Tekhnol.*, **44**, No. 1: 79–95 (2022); https://doi.org/10.15407/mfint.44.01.0079
113. S.P. Chenakin, B.N. Mordyuk, and N.I. Khripta, *Vacuum*, **210**: 111889 (2023); https://doi.org/10.1016/j.vacuum.2023.111889
114. H. Nikiforchyn, V. Kyryliv, O. Maksymiv, Z. Slobodyan, and O. Tsyrulnyk, *Nanoscale Res. Lett.*, **11**: 51 (2016); https://doi.org/10.1186/s11671-016-1266-3
115. R. Hossain, F. Pahlevani, E. Witteveen, A. Banerjee, B. Joe, B.G. Prusty, R. Dippenaar, and V. Sahajwalla, *Sci. Rep.*, **7**: 13288 (2017); https://doi.org/10.1038/s41598-017-13749-7
116. H. Nikiforchyn, V. Kyryliv, and O. Maksymiv, *Nanoscale Res. Lett.*, **12**: 150 (2017); https://doi.org/10.1186/s11671-017-1917-z
117. J. Du, L. Chen, H. Li, Y. Tan, T. Sun, Y. Yang, C. Hua, W.J. Yu, and X. Huang, *Mater. Today Commun.*, **36**: 106886 (2023);

https://doi.org/10.1016/j.mtcomm.2023.106886
118. L. Nánai, R. Vajtai, and T.F. George, *Thin Solid Films*, **298**: 160–164 (1997); https://doi.org/10.1016/S0040-6090(96)09390-x
119. H. Hagino, S. Shimizu, H. Ando, and H. Kikuta, *Precis. Eng.*, **34**: 446–452 (2010); https://doi.org/10.1016/j.precisioneng.2009.11.001
120. F. Klocke, M. Schulz, and S. Grafe, *Coatings*, **7**: 1357–1366 (2017); https://doi.org/10.3390/coatings7060077
121. K. Obergfell, V. Schulze, and O. Vohringer, *Mater. Sci. Eng.*, **355**: 348–356 (2003); https://doi.org/10.1016/S0921-5093(03)00099-6
122. H.W. Zhang, S. Ohsaki, S. Mitao, M. Ohnuma, and K. Hono, *Mater. Sci. Eng. A*, **421**: 191–199 (2006); https://doi.org/10.1016/j.msea.2007.11.081
123. M. Freisinger, H. Rojacz, A. Trausmuth, and P. H. Mayrhofer, *Metallogr. Microstruct. Anal.*, **12**: 515–527 (2023); https://doi.org/10.1007/s13632-023-00967-x
124. V.A. Lobodyuk, Y.Y. Meshkov, and E.V. Pereloma, *Metall. Mater. Trans. A*, **50**: 97–103 (2019); https://doi.org/10.1007/s11661-018-4999-z
125. P.D. Babu and P. Marimuthu, *Emerg. Mater. Res.*, **8**: 1–18 (2019); https://doi.org/10.1680/jemmr.16.00145
126. K. Bhattacharya, S. Conti, G. Zanzotto, and J. Zimmer, *Nature*, **428**: 55–59 (2004); https://doi.org/10.1038/nature02378
127. J.-S. Chen, Z.-X. Li, Y.-J. Chu, J. Chen, and X.-J. Shen, *Met. Mater. Int.*, **28**: 2318–2329 (2022); https://doi.org/10.1007/s12540-021-01148-7
128. R. Li, Y. Jin, Z. Li, and K. Qi, *J. Mater. Eng. Perform.*, **23**: 3085–3091 (2014); https://doi.org/10.1007/s11665-014-1146-x
129. F. Lusquicos, J.C. Conde, S. Bonss, A. Riveiro, F. Quintero, R. Comesaca, and J. Pou, *Appl. Surf. Sci.*, **254**: 948–954 (2007); https://doi.org/10.1016/j.apsusc.2007.07.200
130. B. Peeters, J. Bouquet, O. Malek, A. Van Vlierberghe, and B. Lauwers, *Procedia Manuf.*, **43**: 103–110 (2020); https://doi.org/10.1016/j.promfg.2020.02.120
131. T. Arai, *Int. J. Autom. Technol.*, **14**: 534–545 (2020); https://doi.org/10.20965/ijat.2020.p0534
132. C. Chena, X. Zeng, Q. Wang, G. Liana, X. Huanga, and Y. Wang, *Opt. Laser Technol.*, **124**: 105976 (2020); https://doi.org/10.1016/j.optlastec.2019.105976
133. K.-H. Lee, S.-W. Choi, T.-J. Yoon, and C.-Y. Kang, *J. Weld. Join.*, **34**: 75–81 (2016); https://doi.org/10.5781/JWJ.2016.34.1.75
134. G. Tani, A. Fortunato, A. Ascari, and G. Campana, *CIRP Ann. Manuf. Technol.*, **59**: 207–210 (2010); https://doi.org/10.1016/j.cirp.2010.03.077
135. M.H. Farshidianfar, A. Khajepouhor, and A. Gerlich, *Surf. Coat. Technol.*, **315**: 326–334 (2017); https://doi.org/10.1016/j.surfcoat.2017.02.055
136. F. Qiu and V. Kujanpää, *Mechanika*, **17**, No. 3: 318–323 (2011); https://doi.org/10.5755/j01.mech.17.3.510
137. R.J.B. De Oliveira, R.H.M. de Siqueira, and M.S.F. de Lima, *Int. J. Surf. Sci. Eng.*, **12**: 161–170 (2018); https://doi.org/10.1504/IJSURFSE.2018.091231

138. F. Qiu and V. Kujanpää, *Surf. Eng.*, **28**, No. 8: 569–575 (2012); https://doi.org/10.1179/1743294412Y.0000000034
139. P. Sancho, M.A. Montealegre, J. Dominguez, P. Alvarez, and J. Isaza, *J. Laser Appl.*, **30**: 032507 (2018); https://doi.org/10.2351/1.5040647
140. S. Martínez, A. Lamikiz, E. Ukar, I. Tabernero, and I. Arrizubieta, *Appl. Therm. Eng.*, **98**: 49–60 (2016); https://doi.org/10.1016/j.applthermaleng.2015.12.037
141. M.S. Raza, S. Datta, K. Vivekanand, and P. Saha, *J. Mater. Eng. Perform.*, **28**: 1873–1883 (2019); https://doi.org/10.1007/s11665-019-03943-1
142. S. Liu, J. Zhu, X. Lin, X. Wang, and G. Wang, *Mater. Sci. Eng. A*, **799**: 140164 (2021); https://doi.org/10.1016/j.msea.2020.140164

Received 07.08.2024
Final version 04.11.2024

Д.А. Лесик[1,2,3], Б.М. Мордюк[2,4], В. Алнусірат[5], С. Мартінез[3], В.В. Джемелінський[1], О.О. Гончарук[1], П.В. Кондрашев[1], Ю.В. Ключников[1], А. Ламікіз[3]

[1] Національний технічний університет України «Київський політехнічний інститут імені Ігоря Сікорського», Берестейський проспект, 37, 03056 Київ, Україна
[2] Інститут металофізики ім. Г.В. Курдюмова НАН України, бульв. Академіка Вернадського, 36, 03142 Київ, Україна
[3] Університет Країни Басків, Площа Інженера Торреса Кеведо, 1, 48013 Більбао, Іспанія
[4] Інститут електрозварювання ім. Є.О. Патона НАН України, вул. Казимира Малевича, 11, 03150 Київ, Україна
[5] Прикладний університет Аль-Балка, вул. Салт, 33, 19117 Ес-Салт, Йорданія

УЛЬТРАЗВУКОВЕ ФІНІШНЕ ОБРОБЛЕННЯ СТАЛІ 45, ЗМІЦНЕНОЇ ЛАЗЕРНИМ ТЕРМООБРОБЛЕННЯМ ВОЛОКОННИМ ЛАЗЕРОМ І СКАНУВАЛЬНОЮ ОПТИКОЮ: ІНДУКОВАНЕ ШАРУВАТОЮ СТРУКТУРОЮ ЗМІЦНЕННЯ ТА ПОЛІПШЕНА МОРФОЛОГІЯ ПОВЕРХНІ

Нині поява нових технологій опосередковано висуває підвищені вимоги до звичайних методів і матеріалів. Огляд літератури показує, що комбіновані термомеханічні процеси поверхневого зміцнення й оброблення з використанням висококонцентрованих джерел енергії є перспективними для підвищення цілісності поверхні й експлуатаційних властивостей конструкційних сталей. Деякі пов'язані з поверхнею та мікроструктурні чинники можна розглядати як вирішальні для поліпшення властивостей, а саме: шорсткість поверхні та хвилястість, розмір зерна та фазовий склад, залишкові макронапруження та мікротвердість. Авторами лазерне термічне оброблення (ЛТО), а потім ультразвукове ударне оброблення (УЗУО), також відоме як високочастотне механічне проковування, було послідовно застосовано для оброблення сталі 45, щоб визначити ефективність їхнього сукупного впливу. Приповерхневу мікроструктуру, утворену комбінованим ЛТО+УЗУО-обробленням, досліджено за допомогою оптичної мікроскопії, трансмісійної електронної мікроскопії та рентгенівського дифракційного аналізу. Також оцінено поверхневі залишкові

макронапруження, мікротвердість, шорсткість і хвилястість. Показано, що комбіноване ЛТО + УЗУО-оброблення поверхні спричиняє фазове перетворення й інтенсивну пластичну деформацію, зумовлюючи пошарове зміцнення та подрібнення зернистої структури у приповерхневих шарах середньовуглецевої сталі. Підповерхневу мікротвердість на глибині до ≈50 мкм після комбінованого оброблення було значно збільшено (>10 ГПа) за рахунок інтенсивної пластичної деформації ЛТО-сформованих мартенситних голок, що забезпечує нанорівноважну зернисту мікроструктуру в приповерхневому шарі. Глибина зміцнення (140–440 мкм) у зразках, оброблених ЛТО + УЗУО, залежить від швидкості ЛТО (40–140 мм/хв) і температури нагрівання (1200–1300 °С) сканувальним лазерним променем. Крім того, якщо брати до уваги поверхневі залишкові макронапруження стиснення (>400 МПа), більш гладкий мікрорельєф на поверхні та понижені параметри шорсткості (Ra < < 0,5 мкм), сформовані УЗУО, очікується поліпшення функціональності досліджуваної сталі. Комбінований процес лазерно-ультразвукового поверхневого зміцнення й оздоблення можна використовувати для оброблення великогабаритних сталевих виробів.

Ключові слова: сталь 45, комбіноване поверхневе оброблення, лазерне зміцнення фазовим перетворенням, ультразвукове оздоблювання, градієнтна структура, наноструктурування поверхні, морфологія поверхні.